

# THE WARPS X-RAY SURVEY OF GALAXIES, GROUPS AND CLUSTERS – I. Method and first results

C.A. Scharf <sup>1</sup>, L.R. Jones <sup>1</sup>

Lab. for High Energy Astrophysics, Code 660, NASA/Goddard, Greenbelt MD 20771,  
USA, email: caleb@amadeus.gsfc.nasa.gov, lrj@clopper.gsfc.nasa.gov

H. Ebeling

Institute of Astronomy, Madingley Road, Cambridge CB3 0HA, UK *and* present address  
Institute for Astronomy, 2680 Woodlawn Dr, Honolulu HI 96822, USA, email:  
ebeling@marvin.ifa.hawaii.edu

E. Perlman <sup>2</sup>

Lab. for High Energy Astrophysics, Code 660, NASA/Goddard, Greenbelt MD 20771,  
USA, email: perlman@baley.gsfc.nasa.gov

M. Malkan

Dept. of Astronomy, UCLA, Los Angeles, CA 90024, USA, email:  
malkan@bonnie.astro.ucla.edu

and

G. Wegner

Dept. of Physics & Astronomy, Dartmouth College, 6127 Wilder Lab., Hanover, NH 03755,  
USA, email: wegner@kayz.dartmouth.edu

Received \_\_\_\_\_; accepted \_\_\_\_\_

---

<sup>1</sup>NRC Research Associate

<sup>2</sup>USRA

## ABSTRACT

We have embarked on a survey of *ROSAT* PSPC archival data with the aim of detecting *all* significant surface brightness enhancements due to sources in the innermost  $R \leq 15$  arcmin of the PSPC field of view in the energy band 0.5 – 2.0 keV. This project is part of the Wide Angle ROSAT Pointed Survey (WARPS) and is designed primarily to measure the low luminosity, high redshift, X-ray luminosity function of galaxy clusters and groups. The approach we have chosen for source detection [Voronoi Tessellation and Percolation (VTP)] represents a significant advance over conventional methods and is particularly suited for the detection and accurate quantification of extended and/or low surface brightness emission which could otherwise be missed or wrongly interpreted. We also use energy dependent exposure maps to estimate the fluxes of sources which can amount to corrections of as much as 15%. In an extensive optical follow-up programme we are identifying galaxies, groups and clusters at redshifts ranging from  $z \sim 0.1$  to  $z \sim 0.7$ .

In this paper we present our method and its calibration using simulated and real data. We present first results for an initial 91 fields (17.2 deg<sup>2</sup>) at detected fluxes  $> 3.5 \times 10^{-14}$  erg s<sup>-1</sup> cm<sup>-2</sup> (the WARPS-I survey). We find the sky density of extended objects to be in the range 2.8 to 4.0 ( $\pm 0.4$ ) deg<sup>-2</sup>. A comparison with a point source detection algorithm demonstrates that our VTP approach typically finds 1-2 more objects deg<sup>-2</sup> to this detected flux limit, suggesting that the conventional method fails to detect a significant fraction of extended objects. The surface brightness limit of the WARPS cluster survey is  $\sim 1 \times 10^{-15}$  erg sec<sup>-1</sup> cm<sup>-2</sup> arcmin<sup>-2</sup>, approximately 6 times lower than the Extended Medium Sensitivity Survey (EMSS). The WARPS LogN-LogS (which currently represents a lower limit) shows a significant excess over previous

measurements for  $S \gtrsim 8 \times 10^{-14} \text{ erg sec}^{-1} \text{ cm}^{-2}$ . We attribute this mainly to a larger measured flux from extended sources as well as new detections of low surface brightness systems in the WARPS.

*Subject headings:* galaxies: clusters of - Xrays: sources - cosmology : surveys

## 1. Introduction

Hierarchical models of structure formation in the Universe (such as Cold Dark Matter (CDM) cosmologies) predict the basic evolutionary properties of gravitationally bound aggregates. Clusters of galaxies are the largest such objects to have already decoupled from the Hubble expansion and therefore offer a unique opportunity to evaluate the fundamental properties of the Universe. The dominant baryonic mass component in galaxy clusters is observed to be in the form of hot ( $10^7 - 10^8$  K) intra-cluster gas ( $\sim 90\%$  of the luminous mass) emitting radiation through thermal bremsstrahlung with some contribution from thermal line emission. We therefore expect the X-ray luminosity to be positively correlated with the system mass (assuming a constant baryon mass fraction, see e.g. White et al 1993). Since the measurement of cluster X-ray luminosity is relatively easy, it follows that to investigate the nature of clusters and their formation we should choose a primary selection method based on X-ray observations.

In the past, selection effects have beset optical surveys because of the projection of background and foreground galaxies on the cluster, sometimes leading to false identifications (e.g. Frenk et al 1990), particularly for poor clusters at high redshift, where the contrast with the background galaxy surface density is low. Even with a knowledge of the line-of-sight dynamics of a system it is only possible to assign probabilities for individual objects to belong (gravitationally) to a cluster or group of galaxies. X-ray surveys suffer less from such problems. Since the X-ray surface brightness is proportional to the square of the density of the hot gas within the cluster, the contrast with respect to the unresolved X-ray background is high. X-ray observations also provide information about the potential size and shape leading to much less ambiguous identification of real physical systems <sup>3</sup>.

---

<sup>3</sup> With sufficiently good spectral resolution and signal-to-noise (such as that provided by ASCA, Tanaka et al 1994) one could also determine the velocity distance *of the cluster*

Well selected catalogues of galaxy clusters can then be used to investigate the evolution of the cluster X-ray luminosity function, the morphology and substructure of clusters, the temperature evolution of the gas component, and the evolution of the optically observed galaxy population.

What do we expect the X-ray cluster evolution to be in a hierarchical model ? It would be fair to say that both the observational and theoretical situation are still uncertain. Modeling of the gravitational instability and gas hydrodynamics of clusters has been pursued with semi-analytic methods (Kaiser 1991) and numerical simulation (Evrard 1990, Bryan et al 1994a, Cen & Ostriker 1994, Kang et al 1994 ). From such studies it is evident that the evolutionary properties of clusters are sensitive to both the assumed 'internal' cluster physics (e.g. the presence or absence of cooling flows or feedback mechanisms) as well as the 'external' influence of the underlying cosmological model (e.g. Friedmann model parameters and the power spectrum of mass fluctuations). However, in the case of relatively simple 'internal' cluster physics (e.g. shock heating during gravitational collapse as a dominant mechanism) and a standard CDM cosmology there is a prediction of negative evolution (i.e. a decrease with redshift) in the number density of the *most luminous* clusters (with  $L_x > 5 \times 10^{44}$  erg s<sup>-1</sup> ).

Current surveys broadly confirm this scenario. The EMSS cluster sample of Henry et al (1992) showed evidence (at the  $3\sigma$  level) of negative evolution in the cluster X-ray luminosity function (XLF), with fewer high luminosity clusters at redshifts  $0.3 < z < 0.6$  than at  $0.14 < z < 0.2$ . At lower redshifts, the XBACS and BCS cluster samples recently compiled by Ebeling et al (1996a,b), based on ROSAT All-Sky Survey data, show little evolution of the Schechter function XLF within a redshift of  $z = 0.3$  (although the small amplitude

---

*potential* directly, using (for example) the Fe K- $\alpha$  line, rather than taking the mean over individual galaxies which contains shot noise.

of negative evolution actually measured is statistically highly significant). The earlier detection of evolution at  $z < 0.2$  by Edge et al (1990) has been shown to be due to an unfortunate sampling of clusters at  $z = 0.1$  to  $0.15$ , rather than to evolution (Ebeling et al 1995). At high redshifts ( $0.2 < z < 0.6$ ) and lower luminosities, Castander et al (1995) find evidence for strong negative evolution. However, this result is based on only 13 clusters, and the sample completeness is unclear (see also Section 5 below). Existing X-ray selected surveys have not probed the low-luminosity regime beyond  $z \sim 0.15$ , except for the small sample of Castander et al (1995).

The slope of the cluster XLF steepened with redshift in the EMSS survey of Henry et al (1992) such that at lower luminosities (around  $10^{44}$  erg  $s^{-1}$ ) no evolution was required. If the steep slope of the EMSS high redshift XLF is extrapolated to still lower luminosities ( $L_X < 10^{44}$  erg  $s^{-1}$ ), positive evolution of low luminosity clusters is predicted, with large numbers ( $\sim 8 \text{ deg}^{-2}$ ) of  $z > 0.2$  clusters at low X-ray fluxes ( $> 3 \times 10^{-14}$  erg  $\text{cm}^{-2} \text{ s}^{-1}$ ). Accurate measurements of the high redshift XLF would allow the *form* of the XLF evolution to be determined via the position of the Schechter function break. This would help discriminate between luminosity and density evolution, and discriminate between different hierarchical models, e.g those including a different mix of fundamental particles (e.g. Bryan et al 1994b), a flat power spectrum of the initial fluctuations (Henry et al 1992) and reheating of the intracluster gas at high redshifts (Kaiser 1991). The WARPS cluster survey was designed to make this measurement (Jones et al 1996).

To ensure the completeness of the WARPS sample a source detection method (Voronoi Tessellation and Percolation, VTP) is used which does not discriminate *against* extended sources of low surface brightness and/or irregular morphology. This is especially important because of the evolution that might be expected in properties such as core radius, temperature and morphology. Indeed, cluster morphology has been shown to be a

potentially important cosmological discriminator (Evrard et al 1993, Crone, Evrard & Richstone 1994). While luminous clusters at high redshift ( $z > 0.4$ ) are likely to be detected by standard point source search algorithms, those at lower  $z$  and lower luminosity may be missed altogether by such methods (Section 5) or removed from a flux limited survey due to an incorrectly low flux detection. An analogous situation exists in optically selected galaxy catalogues - a magnitude selected sample with a high surface brightness detection threshold will be incomplete in diameter and vice versa. Such selection effects will bias conventional catalogues against (for example) extended low surface brightness objects and cause fluxes to be incorrectly measured.

In this paper we describe the methods used in the WARPS survey and present its first results. This work is arranged as follows: in Section 2 we present a brief overview of the WARPS survey and the ROSAT PSPC data archive, in Section 3, 3.1, 3.2 and 3.3 we describe the VTP method, the construction of a flux limited catalogue and discuss the accuracy of flux corrections and extended source detection. Section 4 presents the calibration of the survey sky coverage. Section 5 presents a comparison with the results of a conventional detection algorithm. In Section 6 we discuss the current results and in Section 6.1 present a LogN-LogS for WARPS-I. In Section 7 we summarize this paper and present conclusions.

## 2. The WARPS survey and the ROSAT data

The WARPS survey is based on archival ROSAT Position Sensitive Proportional Counter (PSPC) X-ray data. The aim of the WARPS cluster survey is to obtain a well-calibrated, complete sample of all sources which emit X-rays from hot gas trapped in a gravitational potential, from single galaxies to rich clusters. The X-ray images are searched for serendipitous sources using a surface brightness limit, and those sources with detected

flux  $> 3.5 \times 10^{-14}$  erg s $^{-1}$  cm $^{-2}$  (0.5-2 keV) are classified as extended or point-like. In an ongoing optical follow-up programme of the extended sources and selected point-like sources (specifically those with galaxy counterparts) we are obtaining both imaging (from archived plate data and deeper CCD data) and spectroscopy data. The followup procedure has been designed to minimize incompleteness and misidentifications of the X-ray source candidates (catalogue in preparation). The spectroscopic redshifts of cluster galaxies will then allow us to determine the XLF and measure its evolution.

The ROSAT PSPC provides a 2 degree diameter field of view with an energy range of 0.1 – 2.4 keV and a modest energy resolution. The relative positional accuracy of the photon coordinates in the instrument plane is 0.5 arcsec. The shape and size of the instrumental point spread function (PSF) depends on both photon energy and off-axis angle. For a photon energy of 1 keV the PSF has a full width half maximum (FWHM) of 25 arcsec on axis and increases in size with off-axis angle to a FWHM of 58 arcsec at 15 arcmin off axis ( Hasinger et al 1993b). We limit our survey to sources within this off-axis angle. We use the 0.5-2 keV band to detect sources rather than the full 0.1-2.4 keV PSPC band in order to (a) reduce the contribution to the background from gas in our Galaxy at  $\sim 10^6$  K, (b) minimize the size of the PSF, and (c) to maximize sensitivity to hard sources such as clusters of galaxies.

There are currently 4768 PSPC fields in the ROSAT archive. Some 1400 fields have exposure times in excess of 8 ksec and we choose this as one criterion for selecting fields our survey. Our field selection is then based on the following general criteria. We first consider fields in which the primary targets are stars or active galactic nuclei (AGN) and which contain no very bright optical objects (typically bright stars which then make optical follow-up difficult). We avoid pointings whose targets are bright clusters since the latter dominate the inner 15 arcmin of the PSPC's field of view and make serendipitous detections

of other objects impossible. This also ensures that our cluster selection is not affected by the known angular correlation between clusters. In this initial survey we have also chosen high galactic latitude ( $|b| > 20^\circ$ ) fields. The observed distribution of Galactic equivalent column densities of neutral hydrogen (all  $< 10^{21} \text{ cm}^{-2}$ ) implies that there should be virtually no absorption in the 0.5-2 keV band used here. The corrections to the measured X-ray fluxes are  $< 2\%$  on all fields and are therefore well within the total flux uncertainties.

In those fields selected we exclude objects within the inner 3 arcmin radius of the field centre since these normally constitute the original targets.

In Figure 1 the positions of the 91 ROSAT fields selected in this initial survey (WARPS-I) are plotted in Galactic coordinates. The size of the points is proportional to the exposure time which ranges from  $\sim 8000$  seconds to  $\sim 48,000$  seconds, with most fields having exposures  $\geq 10,000$  seconds.

### 3. The VTP method

The VTP method of Ebeling (Ebeling 1993, Ebeling & Wiedenmann 1993) is a general method for the detection of non-Poissonian structure in a distribution of points. In the case of a distribution of photons it will detect all regions of enhanced surface brightness (surface density) relative to the Poissonian expectation. While the ROSAT PSPC photons are in fact registered on a finite grid made from 0.5 arcsec ‘pixels’, we can treat the observed photon distribution as unbinned since, at the exposure times typically attained in the pointings, this grid is well sampled only at the positions of the very brightest sources. The VTP method can be summarized as follows. First, for a raw photon distribution (in this case the inner 15 arcmin radius of the *ROSAT* PSPC and a ‘buffer zone’ of photons to 18 arcmin) the unique Voronoi tessellation is determined (when rare multiple photon counts

occur at a grid position, these are flagged and this information is used in the percolation described below). Each photon defines the centre of a cell polygon whose sides form the perpendicular bisectors of the non-crossing vectors joining the nearest neighbour photons which, in turn, represent the vertices of the equivalent Delauney triangulation. These photon cells form the Voronoi tessellation of the field. Since most cells contain only one photon, the surface brightness associated with this photon equals the inverse of the product of cell area and local exposure time. In Figure 2 the Voronoi tessellation or tiling is shown for a typical ROSAT PSPC field. The sources in this field are apparent to the eye as the clusters of small cells.

The PSPC field experiences non-uniform exposure which can vary by as much as 15-20% from the field center to 15 arcmin radius off axis, and by as much as 10-15% between different fields (according to the spacecraft parameters at a given time). Extended sources will therefore also experience non-uniform exposure across their projected surface (for example  $\sim 5\%$  across a 3 arcmin source). To correct for this, we generate exposure maps for each pointing (with  $15'' \times 15''$  resolution pixels) using an algorithm based on the detailed work of Snowden et al (1992). For greater accuracy, exposure maps are constructed in two energy bands ( 0.5-0.9 keV and 0.9-2 keV) and the appropriate map is used to yield an exposure value *for each photon*. Although the mean difference between the global broad band (0.1-2 keV) exposure map and those used here is only  $\sim 5\%$ , the variation between individual maps can be as much as 15%. The final improvement on estimated source fluxes (especially for extended sources) obtained by using the correct exposure maps can therefore be as much as 10-15% when compared to fluxes with only a uniform exposure correction.

The cumulative distribution of the inverse areas of the Voronoi cells can then be compared with that expected from a random (Poisson) distribution and a cutoff can be determined which defines the global background count for that field. A spatial percolation

algorithm is then run on the cells with areas smaller than a given threshold above the background, grouping them according to the excess above the background density and forming sources. The latter two steps are performed in an iterative fashion so that as sources are detected the background estimate is revised and the source groupings redetermined. Typically this requires  $\sim 6$  iterations. Finally, the minimum number of photons required for a true source is calculated (such that we expect 1 fake source in the total survey area) to eliminate background fluctuations. The background level for a given field is then simply the mean surface brightness ( $\sigma_{back}$ ) calculated from all non-source photons.

For each source a series of parameters are then obtained by VTP. In our analysis we use the following: the source position (determined as a weighted sum over photons), the detected source count rate (corrected for the background count rate), the detected source area, the minimal and maximal moments of inertia of the photon distribution, an estimate of the background count, and the probability of the source being a statistical fluctuation (calculated as the probability of the Poisson background producing a fluctuation of that number of photons with local surface brightness above the detection threshold). In addition, the full set of photons associated with each source is stored.

### 3.1. Source deblending

We perform VTP three times for each field using different surface brightness thresholds (denoted as factors of the background surface brightness: 1.0, 1.3 and 1.7; see Section 4). This allows us to distinguish real single sources from those composed of blends of several sources (point-like or extended) and reduces any uncertainties in source identification due to positive background fluctuations which become grouped with source photons.

The first task in the survey (once VTP has been run) is therefore to perform the

deblending and threshold selections. For this purpose we combine an automated deblending procedure with visual inspection of all fields. The deblending algorithm is run over all VTP results. It includes all sources which match the following criteria:

- Sources at threshold 1.0 which do not deblend at higher thresholds, lie within 15 arcmin of the field centre and typically outside the innermost 3 arcmin radius (to avoid target sources) and with an observed count rate of  $> 3 \times 10^{-3}$  ct/s (corresponding to an observed flux limit of  $\simeq 3.5 \times 10^{-14}$  erg s $^{-1}$  cm $^{-2}$ )
- Sources matching the above position and count rate criteria at threshold 1.3 which were parts of blends at 1.0 but do not deblend at threshold 1.7
- Sources matching the position and count rate criteria at threshold 1.7 which were parts of blends at 1.3

This first run of the deblending algorithm provides a list of candidates which is used in a visual inspection of each field. The choices which may then be made are to alter the detection threshold used for either the entire field or for individual objects. The rationale for this is that sometimes objects detected at threshold 1.0 will include (because of the high sensitivity of VTP) photons which are clearly positive noise and act to bias the area estimate of the source (i.e. spurious ‘tails’ of very low surface brightness which become associated with a source). Increasing the threshold removes this noise and typically only removes  $< 10\%$  of the source photons (which will be recovered in the flux correction step detailed below). The threshold used for each source is recorded and used in the correction from detected to total flux as described in Section 3.2.

Figures 3 and 4 demonstrate the differences between the lowest and highest threshold results for the field in Figure 2. Those photons identified as belonging to sources by VTP are plotted in heavy type. Sources typically account for 10-20% of the photons in the

lowest threshold, less in the highest threshold. The sources numbered 2 and 6 in Figure 3 are strong candidates for blends of more than one source when observed at the lowest threshold. In Figure 4 it is apparent that these sources have been deblended at the higher (1.7) threshold.

Clearly there may be cases of real physical systems which contain structure that becomes deblended. However, a visual inspection of all 91 fields revealed only 2 cases where deblending had split up what was probably a single extended object (which had a flux above the survey flux limit) into separate components which fell below the flux limit. These 2 objects were placed back into the survey sample. In addition, since we obtain optical identification for *all* sources (both extended and point-like) likely to be clusters, groups or normal galaxies, we expect to be able to catch such cases, should they occur. As an additional aid in deblending, the WGACAT point source detections ( White, Giommi & Angelini 1994) are plotted as vertical arrows in Figures 3 and 4. Note that, since the WGACAT sources were detected in the broader 0.24-2 keV band, they cannot be compared directly to the VTP detections; a detailed comparison between VTP and conventional detection algorithms is made in Section 5.

### 3.2. Flux determinations

The final list of deblended sources and their respective VTP parameters are then passed to an algorithm which estimates the true flux of the sources. In order to do this, the general nature of VTP must be abandoned and assumptions made about the nature of the sources. We assume that sources are either intrinsically point-like or extended with a surface brightness distribution following a King profile:

$$\sigma(r) = \sigma_0 \left[ 1 + (r/r_c)^2 \right]^{-3\beta+1/2} , \quad (1)$$

where  $\sigma(r)$  is the projected surface brightness at distance  $r$  from the source centre,  $\sigma_0$  is the central surface brightness,  $r_c$  is the core radius, and  $\beta$  has a value of 2/3 ( Jones & Forman 1984). In modeling the PSF we follow Hasinger et al. (1993b).

The VTP algorithm returns estimates of the mean surface brightness of the background, a background corrected estimate of the observed count rate for each detected source, and the area of the source above the surface brightness threshold. From the area we obtain an area equivalent source radius ( $r_{VTP} = \sqrt{A_{VTP}/\pi}$ ). Two flux correction factors are then computed for each source; the first assumes it is point-like. The second assumes it is extended with a King profile (Equation 1) and with a knowledge of the surface brightness threshold we can numerically obtain an equivalent core radius ( $r_c$ ) (corrected for PSF) and the central surface brightness ( $\sigma_0$ ). The true (integral) source count rate (i.e. including the undetected flux below the threshold) is then simply obtained as:

$$s_{true} = 2\pi \int_0^\infty \sigma(r)r dr = \frac{\pi\sigma_0 r_c^2}{3(\beta - 1/2)} . \quad (2)$$

For simulated data (using idealized surface brightness profiles, such as the King profile) the VTP corrected fluxes are accurate for high signal-to-noise sources (described in Section 3.3 and Figure 6). For low signal-to-noise sources the uncertainty in the corrected flux is larger (e.g. Figure 5). Full details of this procedure can be found in Ebeling et al (1996b).

An object is then classified as extended if the ratio of the correction factors  $f = s_{true}/s_{detected}$  for a King profile and a point source, respectively, lies above a critical value. The true count rate is then obtained by multiplying the detected count rate with the appropriate correction factor. Since it is only integral properties that are used, the results

are much more stable to deviations of objects from the assumed ideal than in the fitting procedures used by conventional detection algorithms.

### 3.3. Flux corrections and extents

To test and calibrate the flux correction method described above we have used Monte Carlo simulations of PSPC fields. Sources are simulated with point-like or King profile surface brightness, convolved with the instrumental PSF (for a nominal photon energy of 1 keV) and added to a representative background of Poissonian noise. An ensemble of sources are made for 40 sets of typical intrinsic parameters (extent, flux, off-axis angle) to determine the expected scatter in the VTP estimates. To further mimic the selection of the real survey data we inspect the simulated sources to choose the appropriate surface brightness threshold to use which eliminates false positive noise wings.

In Figures 5(a,b) and 6(a,b) results are presented across a large range of source parameters, from extents of  $\sim 0$  arcsec to 1.5 arcmin and effective fluxes (0.5-2 keV) of  $\sim 6 \times 10^{-14}$  to  $\sim 3.5 \times 10^{-13}$  erg s $^{-1}$ cm $^{-2}$  and for on-axis (circular) and off-axis (triangular) sources. In all plots the ratio of the raw, detected count rates to the true count rate and the ratio of the corrected (see above) count rates to the true count rate are plotted on the y-axes. Multiple points at fixed intrinsic extents (or fluxes) have a range of intrinsic fluxes (or extents).

The effective VTP detected signal-to-noise (as defined in Section 4 below) of a source is a good indicator of the reliability of any flux estimate. The median signal-to-noise of the real X-ray source detections is  $s/n = 8$ , and we use this to divide the simulation results for presentation. The effect of noise is apparent in the larger scatter seen in flux estimates for the low signal-to-noise ( $s/n < 8$ ) sources plotted in Figure 5(a,b) when compared to those

of the high signal-to-noise objects in Figure 6(a,b). For sources of medium to small extent (i.e.  $< 60$  arcsec) with signal-to-noise  $> 8$  we can recover the true flux to within 5-10% over the flux range shown here. For sources of larger extent (of which we might expect to see very few in our survey) the fluxes are systematically underestimated, as expected since more of the flux now lies below our surface brightness limits. For the low signal-to-noise sources ( $s/n < 8$ ) the same general trends are present but dominated by the scatter due to noise. For small extents ( $< 30$  arcsec) we can still recover the true flux of the faintest objects to within 10-20%. To summarize; all recovered count rates are within  $1\text{-}\sigma$  of the nominal count rates, except for highly extended ( $> 1$  arcmin) and/or faint sources.

In determining the flux correction factor we are able to classify objects as extended or point-like using the ratio of the King profile flux correction factor to the point-like flux correction factor  $f_{King}/f_{PS}$  ( $f_{King} = s_{true}/s_{detected}$ ), where  $s_{detected}$  is estimated assuming a King profile,  $f_{PS}$  is the same factor but with  $s_{detected}$  estimated assuming a point source). If this ratio exceeds some value (not necessarily unity, because of noise) then we deduce that the source is best fit by an extended surface brightness profile (through the integral quantities). This extent criterion has been empirically determined from both these simulation results and the survey data itself. If the ratio of the flux correction factors ( $f_{King}/f_{PS}$ ) is *greater* than 1.2 then  $> 90\%$  of on-axis extended sources with intrinsic extent  $r_c \gtrsim 7$  arcsec will be correctly classified as extended, and  $\lesssim 10\%$  of on-axis point-like sources will be mistakenly classified as extended (from simulations of point-like sources). All high signal-to-noise off-axis sources with intrinsic extent  $r_c \gtrsim 20$  arcsec will be correctly classed as extended. In Figure 7(a,b) we summarize the results of applying this classification to the simulation data. The fraction of sources classified as extended is plotted against intrinsic source extent. It is apparent that off-axis extended sources are more likely to be mis-classified. Given that the PSF FWHM (at 1 keV) on-axis is 25 arcsec and increases to 58 arcsec ( Hasinger et al 1993b) at 15 arcmin off-axis we might expect a degradation of the

method, especially at low signal-to-noise.

The optical follow-up observations we perform for all candidates will allow us to reliably identify the few expected mis-classified objects. To our flux limit of  $3.5 \times 10^{-14}$  erg  $\text{s}^{-1} \text{cm}^{-2}$  we do not expect any extended objects (clusters, groups or galaxies) to have core radii of less than  $\simeq 20$  arcsec, based on the canonical range of physical sizes and luminosities (see Figure 8). Our sample of X-ray extended objects will therefore be complete to this flux limit, assuming no evolution in these canonical sources. If, for example, clusters of the same luminosity were physically smaller at higher redshifts, they might not be classified as extended. However, they would be identified correctly as cluster candidates from our optical imaging of point-like X-ray sources.

A visual inspection of a subset of the real data confirms these results. Of the objects classified by eye as extended, 92% (23 of 25) were classified as extended by VTP. Of the objects classified by eye as point-like, 4% were misclassified by VTP. Many of the misclassifications involved two or more close point-like sources, separated by a distance similar to the PSF full width half maximum, too close to be deblended.

#### 4. Sky coverage

In order to correctly evaluate any statistical measurements of the survey sample (such as LogN-LogS, luminosity functions, extent distribution etc.), the effective sky coverage must be known. Since the WARPS uses pointed data each field has a different detection sensitivity to objects of a given extent and flux, according to exposure and background. To estimate this, we have combined an analytic measure of VTP’s detection sensitivity with the results of simulated PSPC data to ensure its validity. On the basis of simulations we have determined that we can parameterize the criterion for for VTP to successfully detect

a real source using a definition of the detected signal-to-noise. The criterion for source detection is then approximated as;

$$\frac{n_{VTP} - n_{back}}{\sqrt{n_{VTP}}} > 3 \quad , \quad (3)$$

where  $n_{VTP}$  is the total number of photons (source and background) that lie within a radius  $r_{VTP}$  which is the equivalent source radius  $\sqrt{A_{VTP}/\pi}$  where  $A_{VTP}$  is the source area within which the surface brightness exceeds the VTP surface brightness threshold  $\sigma_{VTP}$ , which is defined by the background ( $\sigma_{back}$ ) and threshold ( $f_{min}$ );  $\sigma_{VTP} = f_{min}\sigma_{back}$  ( $f_{min} \geq 1.0$ ). If we assume a King profile as in Equation 1 then we can write:

$$r_{VTP} = \left[ r_c^2 \left[ \left( \frac{\sigma_{VTP}}{\tilde{\sigma}_0} \right)^{-2/3} - 1 \right] \right]^{1/2} . \quad (4)$$

Here, however, we have defined the central surface brightness so as to include the background,  $\tilde{\sigma}_0 = (s_{true}/2\pi r_c^2) + \sigma_{back}$ , in units of counts per unit area. The number of photons detected by VTP should then be;

$$n_{VTP}(r_{VTP}) = 2\pi r_c^2 \tilde{\sigma}_0 \left[ 1 - \left( 1 + \left( \frac{r_{VTP}}{r_c} \right)^2 \right)^{-1/2} \right] . \quad (5)$$

Instead of explicitly including the full (numerical) PSF we have included it as a simple ‘blurring’ of the extent (i.e. the effective extent is  $r_c^{eff} = \sqrt{r_c^2 + PSF(\theta)_\sigma^2}$  where  $\theta$  is off-axis angle). This simplification appears justified when results are compared with simulations. Using the exposure and background information (as determined by VTP) for each of the 91 fields used in the survey we then integrate the sky coverage over the radius of each PSPC field, including the PSF variation with off-axis angle, using the criteria described above to determine the detection sensitivity (for a given  $\sigma_0$  and  $r_c$ ). The final result shown in Figure 8 is the combined sky coverage of all fields used in the survey to the limiting threshold ( $f_{min} = 1.0$ ).

In Figure 8 the fractional sky coverage is shown as a function of projected (intrinsic) extent and intrinsic flux, assuming a King profile as in Equation 1. The dashed contour

denotes 1% coverage and indicates that a few deep fields in our survey do indeed allow detections to much lower fluxes. Solid contours run in steps of 10% from 10% to 100% (with increasing weight). For the WARPS-I sample 100% sky coverage corresponds to 17.2 deg<sup>2</sup>.

The near-horizontal dashed, dotted and solid curves at the lower right in Figure 8 are the loci with varying redshift of (respectively) elliptical galaxies (with  $L_x(0.5-2 \text{ keV}) = 1 \times 10^{42} \text{ erg/s}$  and effective core radius  $r_c = 50 \text{ kpc}$ ), groups (with  $L_x(0.5-2 \text{ keV}) = 1 \times 10^{43} \text{ erg/s}$ ,  $r_c = 100 \text{ kpc}$ ) and clusters (with  $L_x(0.5-2 \text{ keV}) = 5 \times 10^{44} \text{ erg/s}$ ,  $r_c = 250 \text{ kpc}$ ) ( $H_0 = 50$ ,  $q_0 = 0$ ). Redshift is therefore increasing right to left along these curves. The vertical dashed line at  $3 \times 10^{-14} \text{ erg s}^{-1} \text{ cm}^{-2}$  (0.5-2 keV) represents the approximate lower flux limit of the survey. The redshifts of the three object types at this flux limit are listed in Figure 8. As discussed elsewhere we have chosen a flux limit in *observed* and uncorrected flux of  $\sim 3.5 \times 10^{-14} \text{ erg s}^{-1} \text{ cm}^{-2}$  (corresponding to a  $3 \times 10^{-3} \text{ ct/s}$  count rate). The true intrinsic flux limit is therefore slightly higher.

Features to note from this plot are a) for these canonical classes of object we always have a sky coverage of  $\sim 60\%$  or better and b) we have good sky coverage ( $\geq 50\%$ ) for moderately bright but very extended sources ( $r_c > 1 \text{ arcmin}$ ) should such low surface brightness objects exist.

In order to check this calculation we have compared it with the results of several hundred simulated objects processed by VTP. These were constructed to have a range of fluxes, extents and off-axis angles. The full PSF (Hasinger et al 1993b) was used to generate the final, simulated PSPC fields. The agreement with simulations is extremely good and confirms the choice of 3 as a signal-to-noise detection criterion. Note that at the survey flux limit the lowest signal/noise of any real source detection in the 91 fields is 4.4, and most sources have a signal/noise  $> 6$ .

In Figure 9 the WARPS fractional sky coverage is shown as a function of redshift for

three classes of object. We have nearly complete sky coverage for clusters with  $L_x$  (0.5 - 2 keV) =  $5 \times 10^{44}$  erg s<sup>-1</sup> and core radius  $r_c = 250$  kpc out to a redshift of  $z \simeq 1$ , with 50% coverage at a redshift of  $z \sim 1.4$ . We have good coverage for groups (or faint, small clusters) of  $L_x$  (0.5-2 keV) =  $1 \times 10^{43}$  erg s<sup>-1</sup> out to  $z \sim 0.2$  (80% coverage) and for galaxies to about  $z \sim 0.1$  (80%). We will use this information in evaluating (for example) the LogN-LogS measured by the WARPS cluster survey. It supports the discussion in Section 1 on why X-ray selected cluster samples have many advantages over optically selected ones. At a redshift of  $\sim 1$  the number density of galaxies on the sky means that the contrast of any cluster is greatly reduced in the optical, whereas the X-ray contrast is still high.

## 5. A comparison with conventional detection methods

An important result of this work is the demonstration that a method such as VTP can detect sources (especially extended, low surface brightness sources) sometimes missed by conventional source detection algorithms (which are known to be less suited to detection of extended objects). Previous work ( Ebeling et al 1996b) has shown that VTP detects more sources than the Standard Analysis Software System (SASS, Voges et al. 1992) in the Rosat All Sky Survey (RASS). In order to better quantify this difference in source detection efficiency for the PSPC fields we have compared our VTP method with a standard sliding cell method. This sliding cell algorithm is publicly available as part of the XIMAGE data analysis package<sup>4</sup> and is referred to as the DETECT algorithm. Briefly, DETECT divides the image field into boxes to make local estimates of the background (rejecting those which deviate significantly from Poisson expectations) and then forms a global background estimate (rejecting the tails of the Gaussian distribution). The sliding cell size is chosen to

---

<sup>4</sup><http://heasarc.gsfc.nasa.gov/docs/xanadu/ximage/node1.html>

optimize signal-to-noise, and corrections are made for dead time, vignetting effects, and the fraction of the source counts that fall outside the box where the net counts are estimated. Count rate errors are included.

We have run DETECT on a subset of our survey fields, in the energy band 0.5-2 keV, and using the default parameters (such as threshold, source probability etc.). In Figures 10,11,12 and 13,14,15 some examples of the problems encountered by conventional techniques are shown.

In Figure 10, the raw photon map for this field is shown, with the Voronoi cells plotted. Many potential sources are apparent to the eye in this crowded field. In Figure 11 the results of running VTP at the lowest threshold (1.0) are presented. Those sources with background corrected counts of less than 20 photons are labeled with ‘X’. The vertical arrows indicate sources found by DETECT. It is clear that there are several places where DETECT and VTP differ. VTP sources 1, 3 and the photons to the North of source 15 are not seen as enhancements by DETECT. In Figure 12 the picture is clearer at the higher VTP threshold of 1.3. Source 19 which was previously blended into source 15 in Figure 11 is now distinct (also see Figure 10) and is a good candidate (given the lower threshold observation) for an extended source, but is completely missed by DETECT.

In Figures 13,14,15 the results for another field are shown in the same format as for Figures 10,11,12. In Figure 14, VTP sources 1, 21,26 and 27 have no DETECT counterparts. In Figure 15, at the higher VTP threshold of 1.3 we can see that these sources are still significant (now numbered 1, 21, 27 and 28 respectively and are good candidates for extended sources (see also Figure 13).

As a further test, DETECT was run with a greatly reduced threshold for source detection in order to see if it could indeed detect the sources seen by VTP at lower surface brightness. Even when the threshold was lowered to a point at which more than twice

the original number of detections were obtained, many VTP sources remained undetected. Furthermore, at this low threshold many of the DETECT sources were clearly spurious, indicating that even if the DETECT parameters could be altered to find the VTP sources it would be difficult to distinguish these from the false detections.

While those fields in Figures 10–12 and 13–15 were chosen specifically to demonstrate the ability of VTP to detect extended sources missed by conventional methods they are not atypical. To quantify the differences we have used a subset of ten fields from the survey across a range of exposure times and backgrounds. Using the VTP and DETECT algorithms we have made two flux limited samples using this subset (to the same flux limit as WARPS-I). To ensure the robustness of the VTP detections we used the results of the 2nd surface brightness threshold only ( $f_{min} = 1.3$ ). As demonstrated in fields 700114 and 600520 above the DETECT algorithm finds fewer objects to a given flux limit. In terms of the number counts of all objects with flux  $\gtrsim 3.5 \times 10^{-14}$  erg s<sup>-1</sup> cm<sup>-2</sup> (0.5-2 keV) VTP finds a number per unit area of  $\simeq 19.7 \pm 2.8$  deg<sup>-2</sup> compared to DETECT which finds  $\simeq 18.1 \pm 2.7$  deg<sup>-2</sup> from the same data. This difference in counts is almost exactly that which would be expected at this flux limit if the additional sources detected by VTP are in fact extended (based on the results of Rosati et al 1995 who use a wavelet method).

While such sliding cell detection methods can be altered to improve their efficiency for extended objects it is clear that in the worst cases they can miss almost *all* fainter extended objects in a flux limited survey. This has profound implications for any survey of faint extended objects which does not use a detection method sensitive to low surface brightness objects. For example, the recent results of Castander et al (1995) (who also survey ROSAT PSPC fields) indicate that to the same flux limit as used here they detect approximately one object per deg<sup>2</sup> *less* than this present work or the work of Rosati et al (1995). This suggests that there may indeed be a difference in the sensitivity of the X-ray

detection methods used.

## 6. Results and Discussion

The WARPS cluster survey has a current sky coverage of 17.2 deg<sup>2</sup>. Using the VTP method this sample (WARPS-I) contains 298 objects (uncorrected for sky coverage) with detected flux  $> 3.5 \times 10^{-14}$  erg s<sup>-1</sup> cm<sup>-2</sup> (0.5-2 keV). There are 58 extended sources according to the criterion used in Section 3.3. The number of misclassified point-like sources is estimated to be  $\approx 5\%$  of the total number of point-like sources (i.e. about 12 sources), giving a possible range of 2.8–4.0 extended objects deg<sup>-2</sup>. The maximum number of misclassified point-like sources, assuming they all have detections of low signal-to-noise (which, in reality, they do not) is 10%, which gives a lower limit of 2.0 extended objects deg<sup>-2</sup>. The combination of a detection method which is unbiased by shape and surface brightness with a rigorous optical follow-up results in an extremely well selected and quantified catalogue well suited to measuring properties such as cluster evolution.

A simple test of the effectiveness of our approach in identifying extended objects can be made by studying the results obtained for known high redshift clusters. In Table 1 below, 4 known clusters spanning redshifts from  $z= 0.13$  to 0.66 were detected by VTP in the PSPC fields and flagged as being extended. The cluster J1836.10RC was detected twice in separate pointings of exposure 21 ksec and 23 ksec. The raw VTP flux was  $2.8 \times 10^{-14}$  erg cm<sup>-2</sup> s<sup>-1</sup> (0.5-2 keV) (55 photons), and the flux variation between observations was 20% or  $1.2\sigma$ , showing a repeatability of the VTP measurements within that expected from Poissonian statistics.

We find a sky density of 2.1–3.1 ( $\pm 0.4$ ) extended objects deg<sup>-2</sup> to an intrinsic (as opposed to detected) flux limit of  $4.5 \times 10^{-14}$  erg s<sup>-1</sup> cm<sup>-2</sup>. This is in good agreement with

the survey of Rosati et al. (1995), although their initial sample contained only 10 extended objects and our numbers are based on a lower limit of 40 extended objects. The survey of Castander et al (1995) which had a similar survey area and a flux limit of  $3 \times 10^{-14}$  erg s $^{-1}$  cm $^{-2}$  found a sky density of  $0.9 \pm 0.25$  extended object deg $^{-2}$ . There is clearly a discrepancy between these observations. We have demonstrated (in agreement with previous works, Ebeling et al 1996b) that the VTP method detects more objects than conventional methods, which were designed with point source detection more in mind. In the extreme case, based on an exact comparison to our flux limit ( $\sim 3.5 \times 10^{-14}$  erg s $^{-1}$  cm $^{-2}$ ) VTP detects some 2 objects deg $^{-2}$  *more* than a sliding cell method. This indicates that a large fraction of extended objects may be missed at this flux limit. Until we have redshifts for these low surface brightness objects we cannot estimate the effect of their exclusion from previous surveys; however we suggest that counts of low luminosity, moderate redshift clusters obtained with non-optimal detection algorithms should not be considered reliable.

### 6.1. Surface brightness limits and LogN-LogS

While often quoted in optical surveys the limiting surface brightness is not generally presented in X-ray surveys. In Figure 16 we present the distribution of surface brightness limits for the WARPS cluster survey fields used in this present work. This is simply determined from the observed background counts in the fields and the VTP surface brightness thresholds. The vertical dot-dashed and dashed lines represent a comparison of the WARPS surface brightness limits with that of the EMSS respectively. For example, a limiting surface brightness of  $1.3 \times 10^{-15}$  erg s $^{-1}$  cm $^{-2}$  arcmin $^{-2}$  (0.5-2 keV) (dot-dashed line in Figure 16) in a typical ROSAT PSPC field with a background level of 3 ct/arcmin $^2$  in 15 ksec exposure corresponds to a two sigma excess over the background in a  $2.4 \times 2.4$  arcmin cell (the EMSS detection cell). To compare this with the limiting surface brightness

in the EMSS, parameters for a typical EMSS field were taken from Gioia et al (1990). For an Einstein IPC exposure of 3.5 ksec and the same  $2.4 \times 2.4$  arcmin cell size containing 9 background counts, a two sigma excess was given by a surface brightness of  $1.4 \times 10^{-14}$  erg  $s^{-1}$   $cm^{-2}$  arcmin $^{-2}$  (0.3-3.5 keV) or  $7.8 \times 10^{-15}$  erg  $s^{-1}$   $cm^{-2}$  arcmin $^{-2}$  (0.5-2 keV) (dashed line in Figure 16), using an EMSS (0.3-3.5 keV) to ROSAT (0.5-2 keV) band conversion factor of 0.55, appropriate for a power law spectrum of energy index 1 or a thermal spectrum of temperature  $kT=6$  keV. The typical WARPS surface brightness limit is therefore  $\approx 6$  times lower than that of the EMSS. We then expect to detect more flux from low surface brightness emission than in (for example) the EMSS.

In Figure 17 we present the first number count results for the WARPS-I cluster survey. The LogN-LogS relationship is shown for the 91 PSPC fields and 298 objects analysed at the time of writing (a total sky coverage of  $17.2$  deg $^2$ ). The 0.5-2 keV count rates were converted to fluxes using a constant factor of  $1.15 \times 10^{-11}$  erg  $s^{-1}$   $cm^{-2}$  (ct  $s^{-1}$ ) $^{-1}$ . This conversion factor is accurate to within 7% for a thermal Raymond-Smith (1977) spectrum of temperature  $kT=1-20$  keV, abundances 0.25-1 times cosmic abundance, and column densities  $1 \times 10^{20}$   $cm^{-2}$  -  $1 \times 10^{21}$   $cm^{-2}$ . These counts include *all* sources (extended or pointlike). The counts have been corrected for sky coverage assuming all sources to be pointlike, this will result in an underestimate of the number counts. The raw flux data points therefore represent a *lower limit*. The initial results for the corrected flux points are shown (with pointlike sky coverage correction) to demonstrate the size of the flux correction. We have also plotted the LogN-LogS relationships found by Hasinger et al (1993a) and Branduardi-Raymont et al (1994) (hereafter BR94), from ROSAT data and Gioia et al (private communication in BR94) from Einstein EMSS data converted to the ROSAT band. The curves represent the LogN-LogS relationships of all sources, as detected with PSF-based detection algorithms.

We see a clear excess at the brighter end compared with other measurements. There are two possible explanations; first, that the VTP method simply detects more objects because it is sensitive across a greater range of surface brightness than other detection methods. Second, that the observed VTP flux is higher for bright extended objects because it includes the signal from the lower surface brightness parts of sources. A combination of these two effects is also likely. This result suggests that a single power law is insufficient to describe the counts over this range in flux ( $\sim 3 - 10 \times 10^{-14}$  erg s $^{-1}$ cm $^{-2}$  (0.5-2 keV)).

If we assume that the deviation from other measurements is due to the improved detection of extended sources (since all detection methods should be essentially equal in the detection efficiency of point-like sources) then we are detecting a population of low surface brightness sources with a density of  $\sim 1$ deg $^{-2}$  at a flux greater than  $\sim 1 \times 10^{-13}$  (with some confidence since we actively avoid fields with known, bright, clusters as targets). Alternatively, if we are not detecting an additional population but rather a greater flux for previously detected objects (presumably extended ones, using the above reasoning) then this amounts to a  $\gtrsim 20\%$  increase in measured flux for objects with flux greater than  $10^{-13}$ . We have made a preliminary investigation of those sources contributing to these higher flux counts which suggests that the excess in our LogN-LogS is indeed due in part to an improved detection of the low surface brightness component of brighter, extended sources.

## 7. Summary and Conclusions

The ability to test cosmological models through detailed studies of galaxy clustering calls for well selected surveys which span the entire range of cluster types. Since the dominant luminous mass component in such systems is hot, X-ray emitting gas this offers an ideal way of selecting objects, it is also free of many of the uncertainties in optically derived catalogues. In order to extend the currently probed section of the cluster population

to lower luminosities and surface brightnesses and higher redshifts we must use general, unbiased source detection methods such as VTP.

The lower limit LogN-LogS of all sources in WARPS-I shows a significant excess in counts for fluxes greater than  $\sim 10^{-13}\text{erg s}^{-1}\text{cm}^{-2}$  (0.5-2 keV) compared to previous works. This excess is consistent with the combined point-like and extended source counts of Rosati et al (1995) and appears to be due to an improved detection of the flux associated with extended sources. We have determined our surface brightness limit to be  $\sim 1 \times 10^{-15}\text{erg s}^{-1}\text{cm}^{-2}\text{ arcmin}^{-2}$  (0.5-2 keV) which is approximately 6 times lower than that of the EMSS, in agreement with our excess counts. On the basis of a pure X-ray classification we determine a sky density of 2.1–3.1 ( $\pm 0.4$ ) extended objects  $\text{deg}^{-2}$  in the present sample with intrinsic flux  $> 4.5 \times 10^{-14}\text{erg s}^{-1}\text{cm}^{-2}$  (0.5-2 keV).

Our survey has complete sky coverage ( $17.2\text{ deg}^2$ ) for rich clusters ( $L_X = 5 \times 10^{44}\text{erg s}^{-1}$ ) to a redshift of 1. At our flux limit of  $3.5 \times 10^{-14}\text{erg s}^{-1}\text{cm}^{-2}$  we can detect (with  $\sim 50 - 60\%$  sky coverage) rich clusters to  $z=1.16$ , groups or poor clusters to  $z=0.23$  and individual galaxies to  $z=0.08$ , assuming the canonical sizes and luminosities of such objects. We have confirmed our detection of extended objects at high redshift by comparison with known clusters (Table 1). Furthermore we find that using the appropriate exposure maps for the ROSAT PSPC fields can improve flux estimates by as much as 15% compared to a uniform correction and can reduce the variations between flux estimates in different fields (if only a standard correction were applied) by as much as 15%.

We have demonstrated that VTP detects more low surface brightness emission than conventional PSF/sliding cell based methods. In the worst cases such methods can miss a large fraction of fainter extended objects in a flux limited survey. This has profound implications for any survey of faint extended objects which does not use a detection method sensitive to low surface brightness objects. For example, the recent results of Castander et

al (1995) (who also survey ROSAT PSPC fields) when compared with the results in this paper or of Rosati et al (1995) suggest a significant difference in the detection sensitivity of the methods used.

Work in progress will address the issues of the cluster LogN-LogS, evolution in the cluster XLF, cluster morphologies and optical classifications using the WARPS-I survey.

### **Acknowledgements**

The data used in this work have been obtained from the High Energy Astrophysics Science Archive Research Center (HEASARC) at NASA Goddard Space Flight Center (<http://heasarc.nasa.gov> address). CAS and LRJ acknowledge Regular and Senior NRC Research Associateships respectively. We acknowledge discussions with Nick White and Richard Mushotzky and thank Nick White, Lorella Angelini and Paolo Giommi for producing WGACAT, on which early work was based.

Table 1: Known clusters detected as extended X-ray sources by VTP

Cluster	Reference	Redshift	Note
Pavo	Griffiths et al 1992	0.13	In Einstein deep survey field
J1836.10RC	Couch et al 1991	0.275	
0055-279	Roche et al 1995	0.56	In SGP field
F1767.10TC	Couch et al 1991	0.664	

## REFERENCES

- Branduardi-Raymont, G., et al., 1994, MNRAS, 270, 947
- Bryan, G.L., Cen, R., Norman, M.L., Ostriker, J.P., Stone, J.M., 1994a, ApJ, 428, 405
- Bryan, G.L., Klypin, A., Loken, C., Norman, M.L., Burns, J.O., 1994b, ApJ, 437, 5
- Castander, F.J., Bower, R.G., Ellis, R.S., et al, 1995, Nature 377, 39
- Cen, R., Ostriker, J.P., 1994, ApJ, 429, 4
- Couch, W.J., Ellis, R.S., Malin, D.F., McLaren, I., 1991, MNRAS, 249, 606
- Crone, M.M., Evrard, A.E., Richstone, D.O., 1994, ApJ, 434, 402
- Ebeling H., 1993, thesis, MPE report no 250, ISSN 0178-0719
- Ebeling H., Wiedenmann G., 1993, Phys. Rev., 47, 704
- Ebeling, H. et al., 1994, in Wide Field Spectroscopy and the Distant Universe, S.J. Maddox & A. Aragon-Salamanca (eds), World Scientific, p. 221
- Ebeling, H. et al., 1996a, Proceedings of "Roentgenstrahlung from the Universe", Wurzburg, Sept 1995.
- Ebeling, H. et al., 1996b, MNRAS in press
- Edge, A.C., Stewart, G.C., Fabian, A.C., Arnaud, K.A., 1990 MNRAS, 245, 559
- Evrard, A.E., 1990, ApJ, 363, 349
- Evrard, A.E., Mohr, J.J., Fabricant, D.G., Geller, M.J., 1993, ApJ, 419, L9
- Frenk, C.S., White, S.D.M., Efstathiou, G., Davis, M., 1990, ApJ, 351, 10
- Gioia, I.M., Maccacaro, T., Schild, R.E., Wolter, A., Stocke, J.T., Morris, S.L., Henry, J.P., 1990, ApJS, 72, 567
- Griffiths, R.E., et al., 1992, MNRAS, 255, 545

- Hasinger, G., Burg, R., Giacconi, R., Hartner, G., Schmidt, M., Trumper, J., Zamorani, G.,  
1993a, A&A, 275, 1
- Hasinger, G., Boese, G., Predehl, P., Turner, T. J., Yusaf, R., George I., Rohrbach G.,  
1993b, MPE/OGIP Calibration memo Cal/Ros/93-015
- Henry, J.P., Gioia, I.M., Maccacaro, T., Morris, S.L., Stocke, J.T., Wolter, A., 1992, ApJ,  
386, 408
- Jones, C., Forman, W., 1984, ApJ, 276, 38
- Jones, L.R., Fong, R., Shanks, T., Ellis, R.S., Peterson, B.A., 1991, MNRAS 249, 481
- Jones, L.R., Scharf, C.A., Perlman, E., Ebeling, H., Malkan, M., Wegner, G., Proceedings  
of "Roentgenstrahlung from the Universe", Wurzburg, Sept 1995.
- Kaiser, N., 1991, ApJ, 383, 104
- Kang, H., Cen, R., Ostriker, J.P., Ryu, D., 1994, ApJ, 428, 1
- Raymond, J.C., Smith, B.W., 1977, ApJS, 35, 419
- Roche, N., Shanks, T., Almani, O., Boyle, B.J., Georgantopoulos, I., Stewart, G.C.,  
Griffiths, R.E., 1995, MNRAS, 276, 706
- Rosati, P., Della Ceca, R., Burg, R., Norman, C., Giacconi, R., 1995, ApJ, 445, L11
- Snowden, S.L, Plucinsky, P.P., Briel, U., Hasinger, G., Pfeffermann, E., 1992, ApJ, 393, 819
- Tanaka, Y., Inoue, H., Holt, S.S., 1994, PASJ, 46, no 3., L37
- Voges, W. et al., 1992, Proceedings of Satellite Symposium 3, ESA ISY-3, p223
- White, N.E., Giommi, P., Angelini, L., 1994, IAU circular 6100, also  
<http://heasarc.gsfc.nasa.gov/StarTrax/Browse.html>
- White, S.D.M., Navarro, J.F., Evrard, A.E., Frenk, C.S., 1993, Nature, 366, 429

**Figure captions:**

**Figure 1:** The 91 ROSAT pointings selected for this initial survey (Aitoff projection in Galactic coordinates). Points are weighted by exposure time. The dotted horizontal lines delimit  $|b| = 20^\circ$ , the hatched line is the equatorial coordinate system equator ( $\delta = 0^\circ$ ).

**Figure 2:** The Voronoi tessellation of a typical ROSAT PSPC photon distribution (the target is a star, HD 173524). Photons are shown as points, the tessellation cells occupy the inner 18 arcmin radius of the field. Sources are immediately apparent to the eye as clusters of small cells.

**Figure 3:** The source photons and sources identified by VTP at threshold 1.0 in the field shown in Figure 2. Heavy points indicate VTP source photons, sources are labelled numerically. The vertical arrows mark the positions of sources from WGACAT (which uses a conventional detection algorithm, in a broader energy band). Note that some VTP sources (such as 2 and 6) are clearly potential blends.

**Figure 4:** The source photons and sources identified by VTP at threshold 1.7 in the field shown in Figure 2. Note that sources 2 and 6 at threshold 1.0 have now been resolved out into sources 2,6,8,9,10 and 11,13,15 respectively.

**Figure 5 a,b:** The mean ratios of detected and corrected count rates to the true count rate of low signal-to-noise ( $s/n < 8$ ) simulated sources plotted against (a) source extent (arcsec) and (b) source count rate. Each point is the mean ratio of the Monte Carlo realisations within a simulation of a given set of parameters. Open symbols represent raw, detected count rates, filled symbols represent count rates corrected as described in Section 4. Circular points denote sources simulated to be on-axis, triangular points denote sources simulated to be 15 arcmin off-axis. Error bars show the  $1\sigma$  scatter.

**Figure 6:** As in Figure 5(a,b) but for high signal-to-noise sources ( $s/n > 8$ ).

**Figure 7 a,b:** The fraction of simulated sources recognized as extended (with an extended source criterion that  $f_{King}/f_{PS} \geq 1.2$ ) is plotted against intrinsic source extent. In a) the results for low signal-to-noise sources ( $s/n < 8$ ) are plotted in b) the results for high signal-to-noise sources ( $s/n > 8$ ) are plotted. Circular symbols represent the results for on-axis sources, triangular symbols represent sources at 15 arcmin off-axis. The symbols are scaled according to the number of source photons.

**Figure 8:** The sky coverage offered by the 91 fields used in this initial survey. Sky coverage is plotted as a function of intrinsic flux and intrinsic, projected extent (assuming a King profile). Contours are drawn at percentage of total survey area. The dashed contour is at a level of 1%, subsequent solid contours (of increasing weight) are 10%,20%... to 100%. The near horizontal *dashed*, *dotted* and *solid* curves at the lower right are the loci with redshift of (respectively) *elliptical* galaxies ( $L_x(0.5-2 \text{ keV}) = 1 \times 10^{42} \text{ erg/s}$ ,  $r_c = 50 \text{ kpc}$ ), *groups* ( $L_x(0.5-2 \text{ keV}) = 1 \times 10^{43} \text{ erg/s}$ ,  $r_c = 100 \text{ kpc}$ ) and *clusters* ( $L_x(0.5 - 2 \text{ keV}) = 5 \times 10^{44} \text{ erg/s}$ ,  $r_c = 250 \text{ kpc}$ ) ( $H_0 = 50$ ,  $q_0 = 0$ ). Redshift is therefore increasing right to left and is different for each curve. The vertical dashed line at  $3.5 \times 10^{-14} \text{ erg sec}^{-1} \text{ cm}^{-2}$  (0.5-2 keV) represents the approximate lower flux limit of the survey. The redshifts of the three object types at this flux limit are listed.

**Figure 9:** The WARPS sky coverage as a function of redshift for three classes of objects: Elliptical galaxies (with  $L_x(0.5-2 \text{ keV}) = 1 \times 10^{42} \text{ erg s}^{-1}$  and effective core radius  $r_c = 50 \text{ kpc}$ ), Groups ( $L_x(0.5-2 \text{ keV}) = 1 \times 10^{43} \text{ erg s}^{-1}$ ,  $r_c = 100 \text{ kpc}$ ) and Clusters (with  $L_x(0.5 - 2 \text{ keV}) = 5 \times 10^{44} \text{ erg s}^{-1}$ ,  $r_c = 250 \text{ kpc}$ ). Light and heavy curves represent cases in which  $q_0 = 0$  and 0.5 respectively. The Hubble constant  $H_0$  (km/s/Mpc) is 50 in all cases.

**Figure 10:** The raw PSPC photons and Voronoi cells for field 700114.

**Figure 11:** The same field (700114) as in Figure 10. VTP source detections are plotted as heavy points, detections are made to the lowest surface brightness threshold used in

the survey. Those VTP sources with background corrected photon counts less than 20 are labelled with ‘X’. Vertical arrows indicate the source detections of the sliding window algorithm.

**Figure 12:** As in Figure 11, but the surface brightness threshold used by VTP is now 1.3.

**Figure 13:** The raw PSPC photons and Voronoi cells for field 600520.

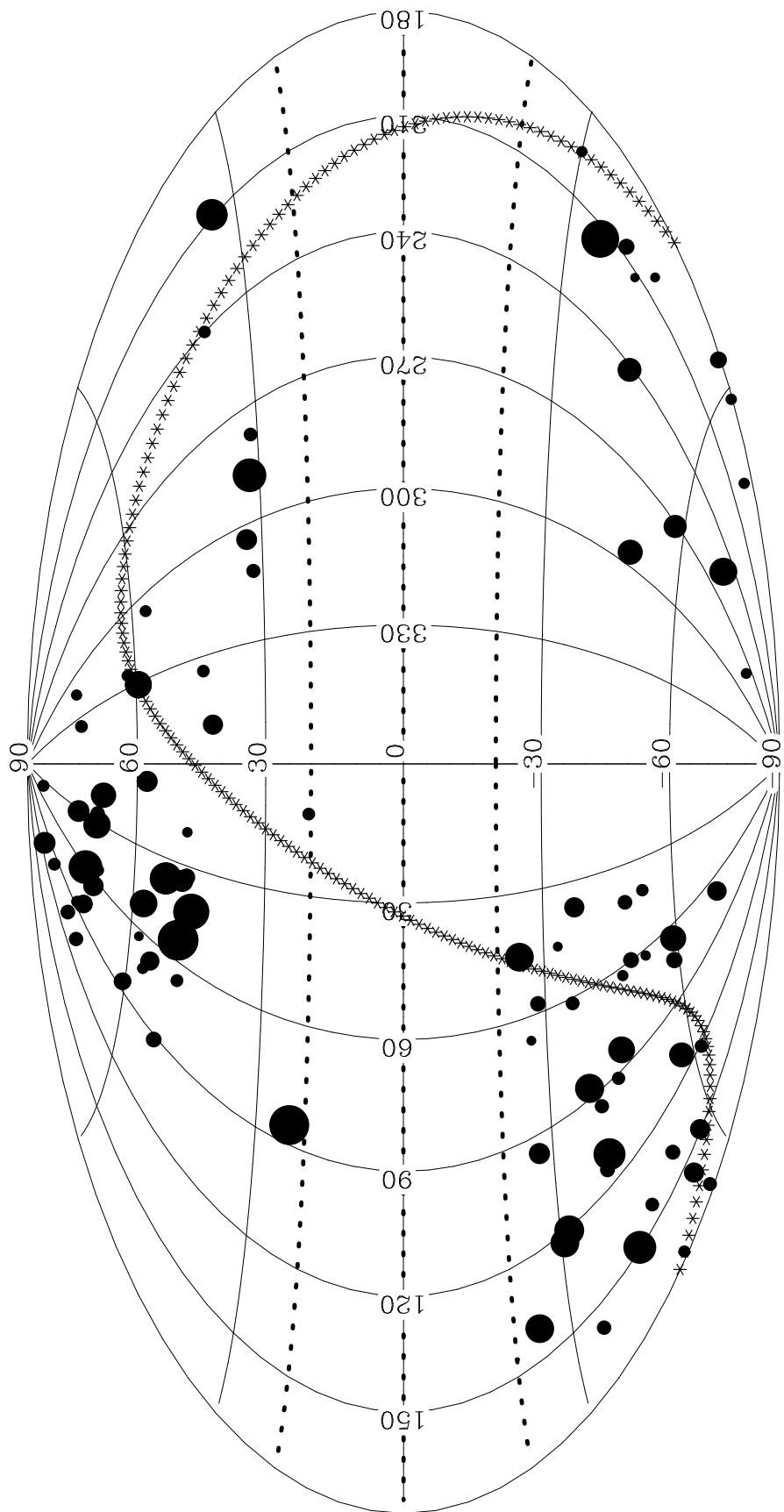
**Figure 14:** The same field (600520) as in Figure 13. VTP source detections are plotted as heavy points, detections are made to the lowest surface brightness threshold used in the survey. Those VTP sources with background corrected photon counts less than 20 are labelled with ‘X’. Vertical arrows indicate the source detections of the sliding window algorithm.

**Figure 15:** As in Figure 14, but the surface brightness threshold used by VTP is now 1.3.

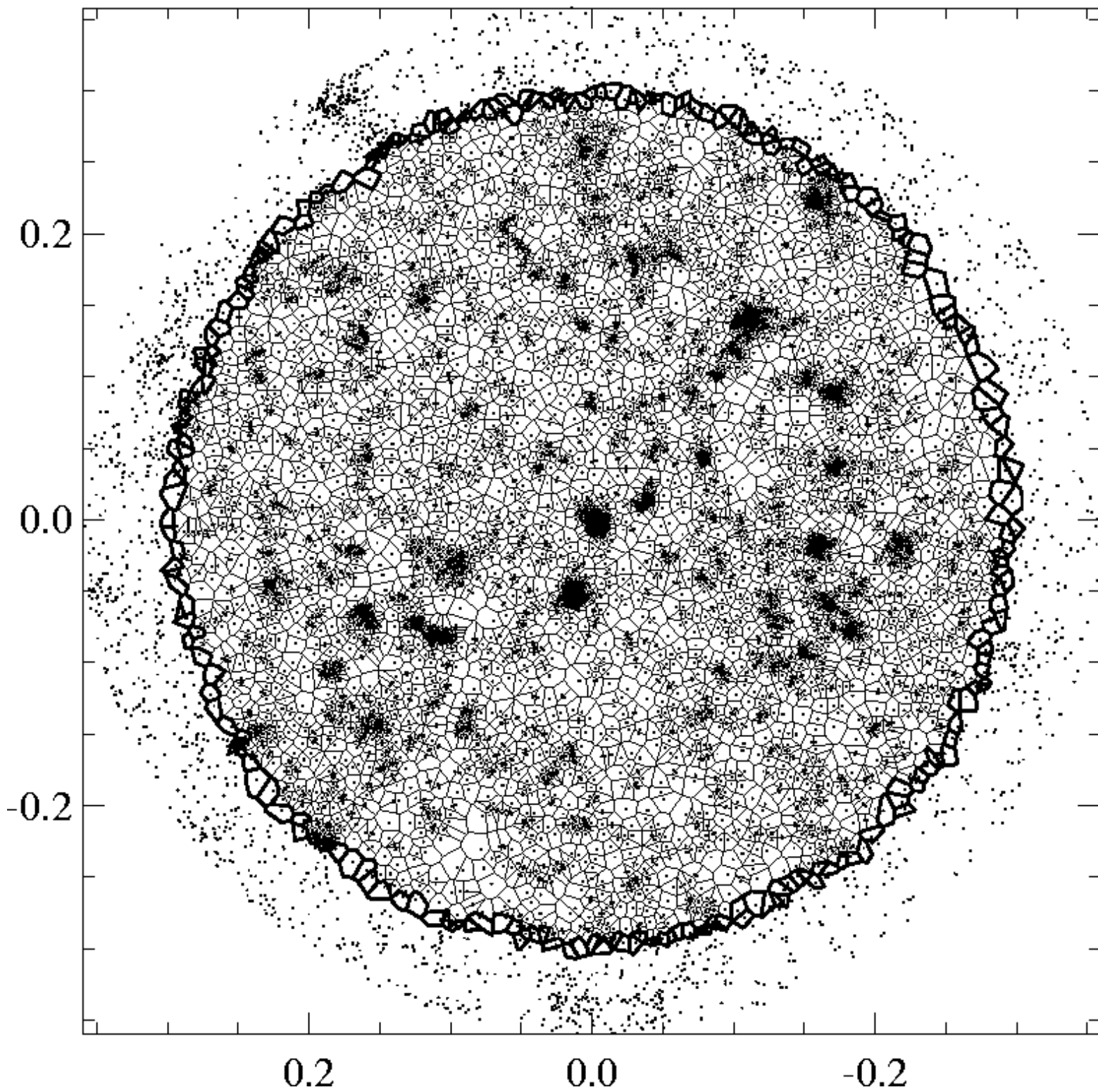
**Figure 16:** The distribution of surface brightness limits in the WARPS cluster survey fields. The spread in values reflects the spread in background counts in the PSPC fields. The vertical dot-dashed line at a surface brightness of  $1.3 \times 10^{-15}$  corresponds to a two sigma surface brightness detection in a square cell (see text) for a typical ROSAT field. The vertical dashed line to the right represents the equivalent significance typical surface brightness detection limit of the EMSS, adjusted to the 0.5-2 keV band. It is  $\sim 6$  times higher than the mean WARPS limit.

**Figure 17:** The LogN-LogS of all sources in the initial WARPS survey (0.5-2 keV). The number counts for raw (corrected only for backgrounds) fluxes (plotted as filled symbols) have been corrected for sky coverage assuming zero object extents, these data points should therefore be considered as lower limits for the survey. The number counts for corrected fluxes (open symbols) have also been corrected for sky coverage assuming zero extent objects. The curves are the results of earlier works, Hasinger et al (ROSAT PSPC data)

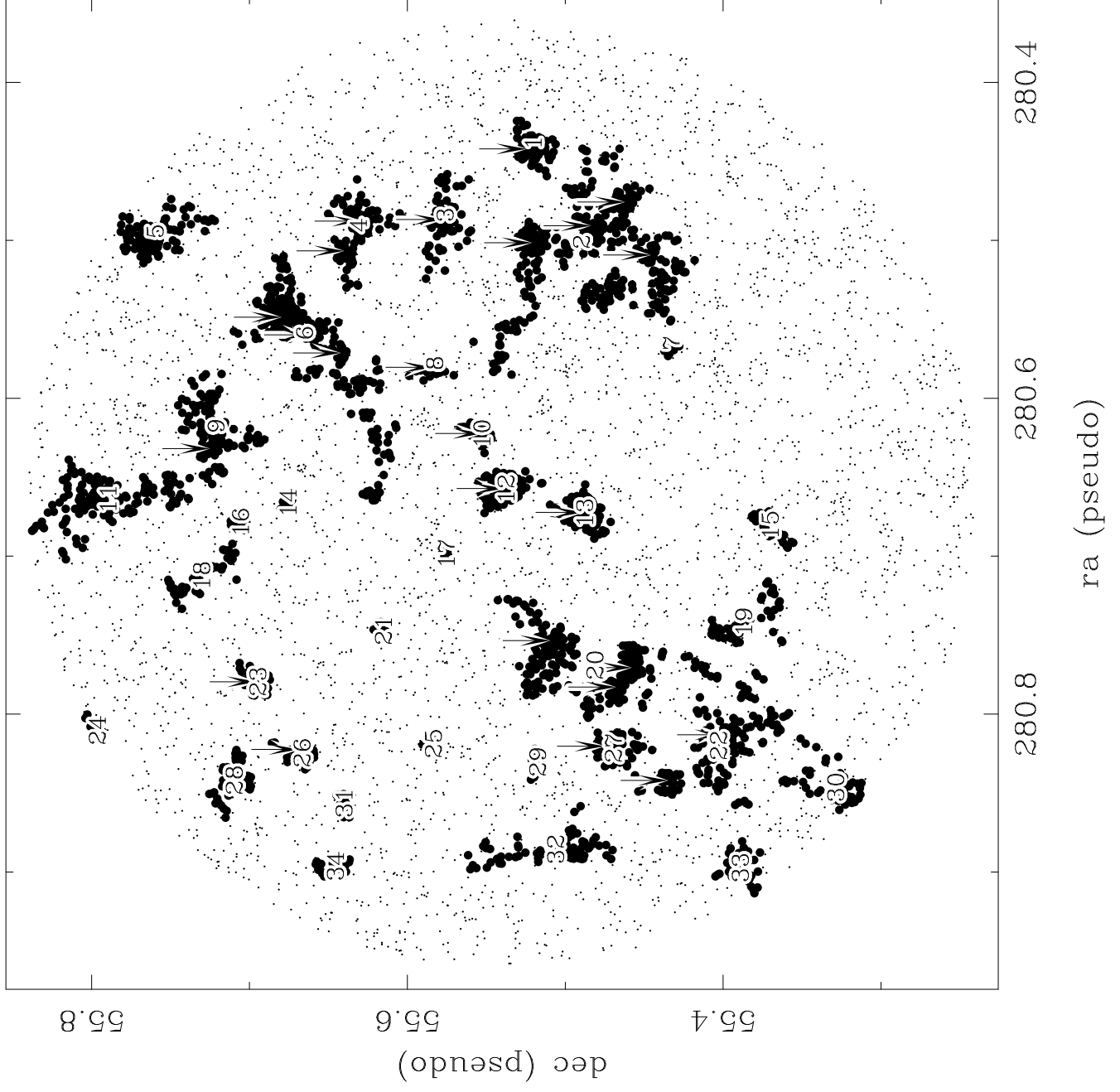
1993a (solid curve), BR (ROSAT data) 1994 (dashed curve) and the Einstein Medium Sensitivity Survey (EMSS) (Gioia et al, private comm. BR94) (dot-dashed curve). Error bars are displayed on only two data points for illustration, since these are integral quantities the errors are not independent. The faintest point for the corrected fluxes is not plotted since the survey limit in detected flux excluded sources which would otherwise have been moved into this bin from fainter fluxes by the flux correction.



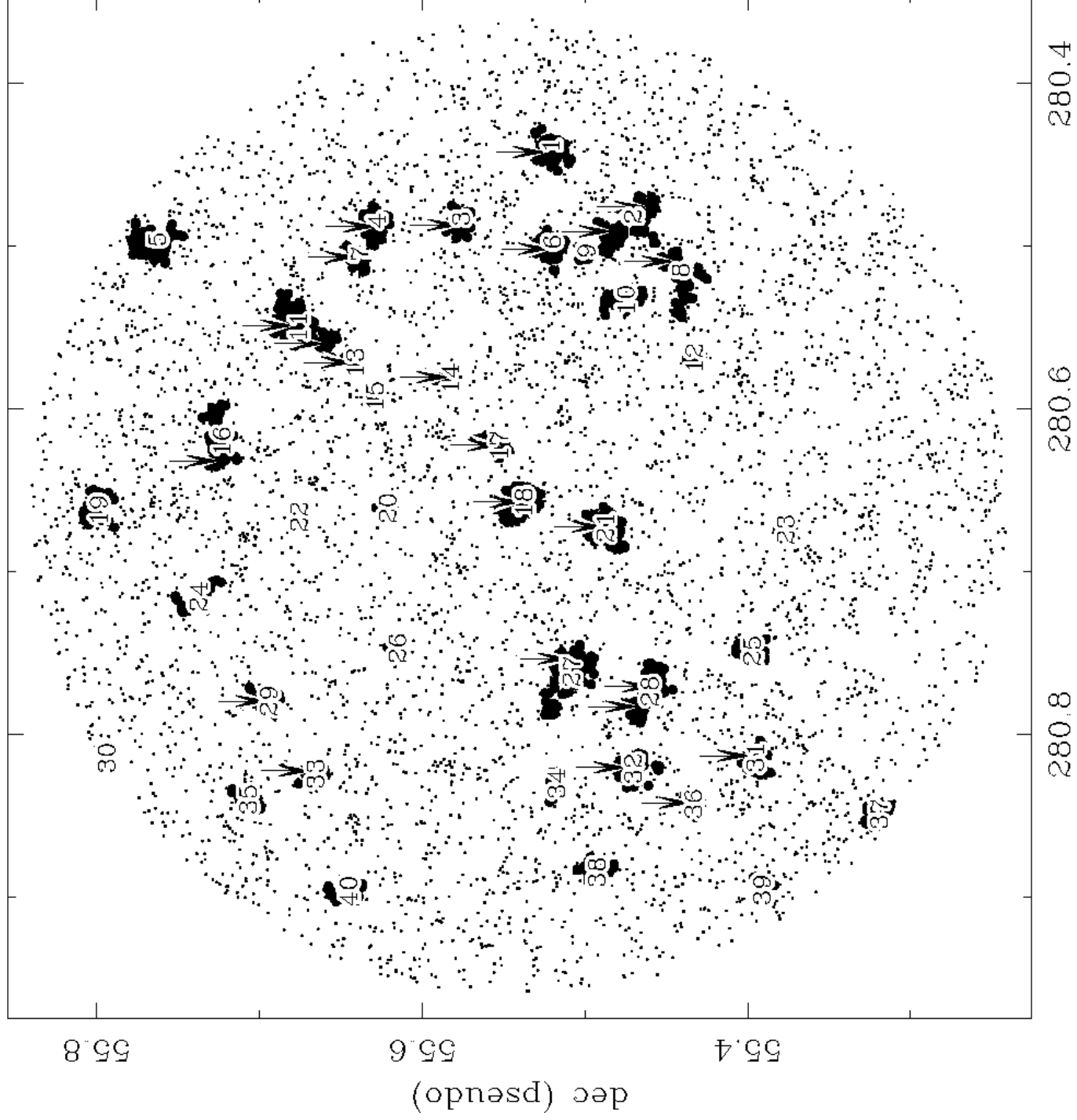
# US201505P.N1



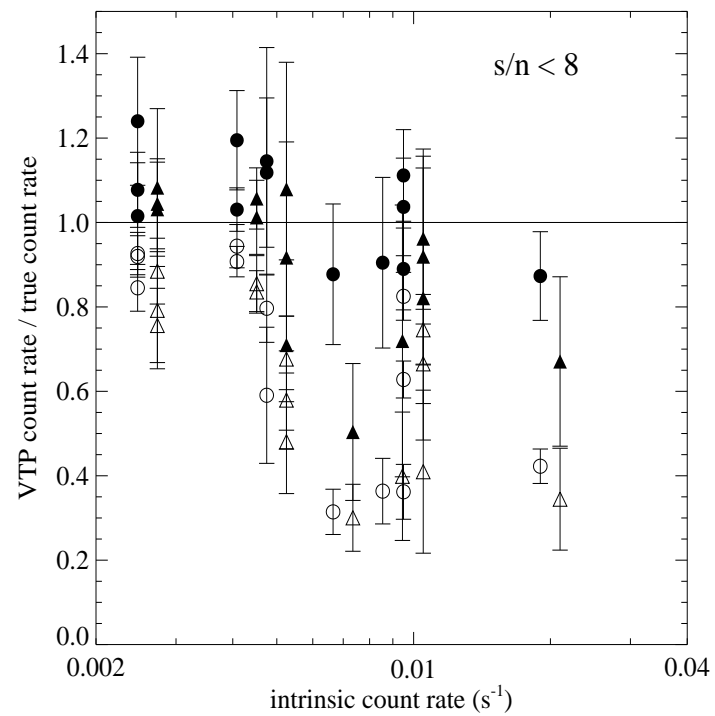
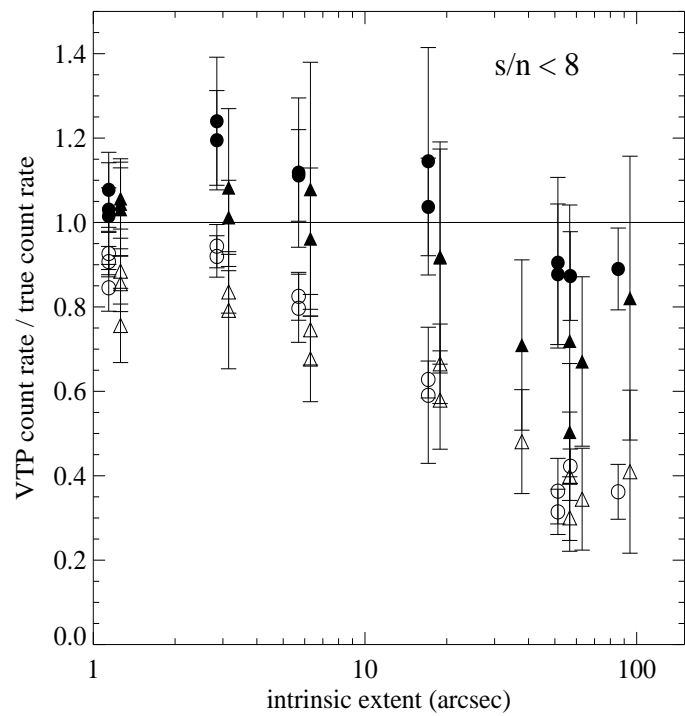
rp201505n00\_1.0

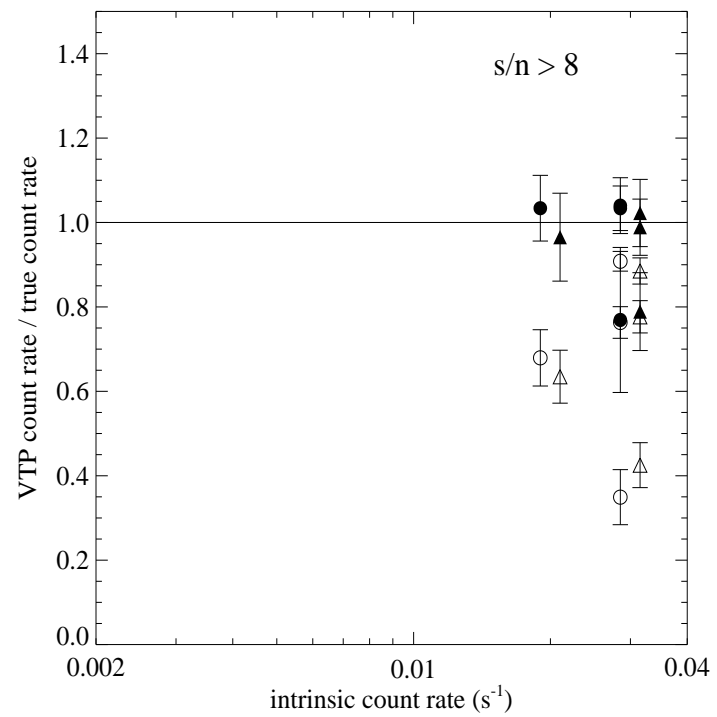
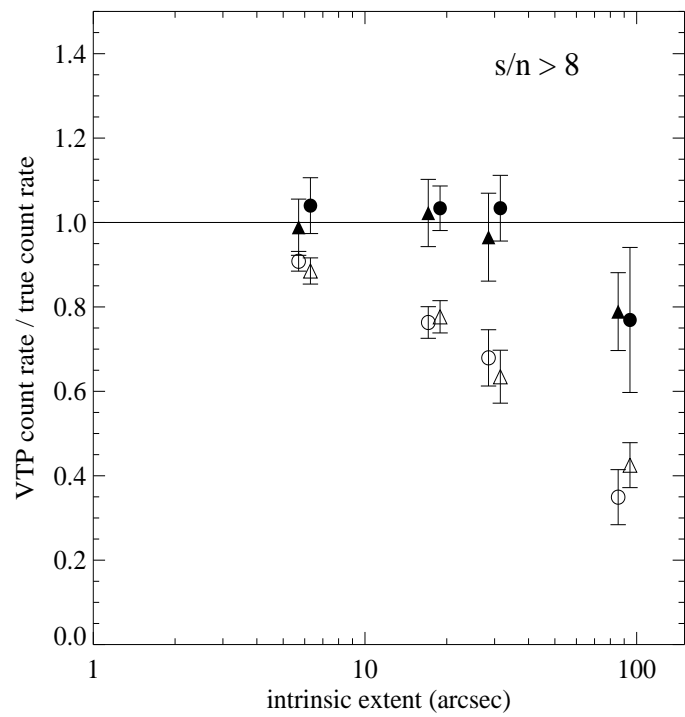


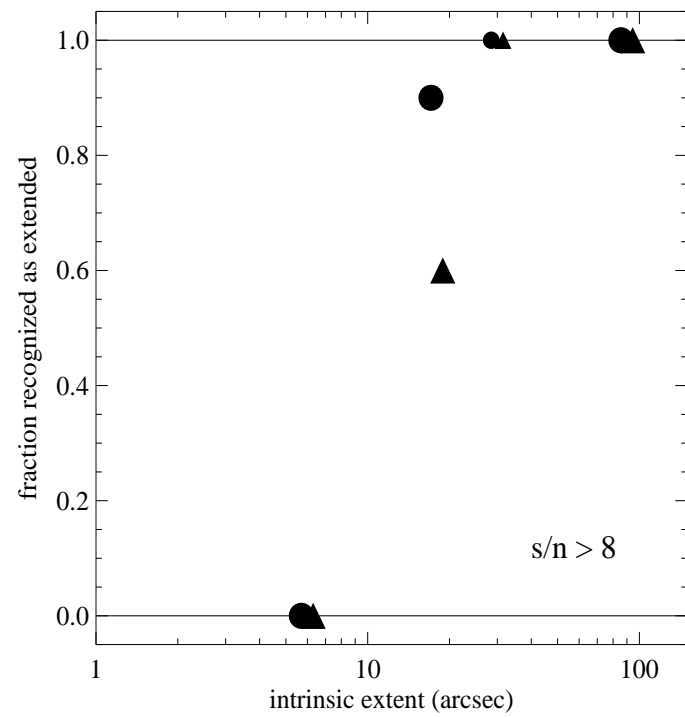
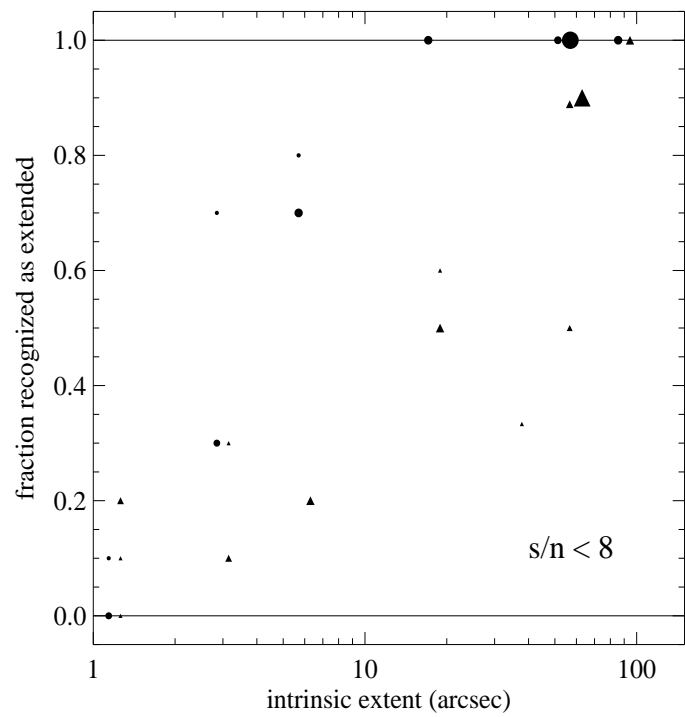
rp201505n00\_1.7



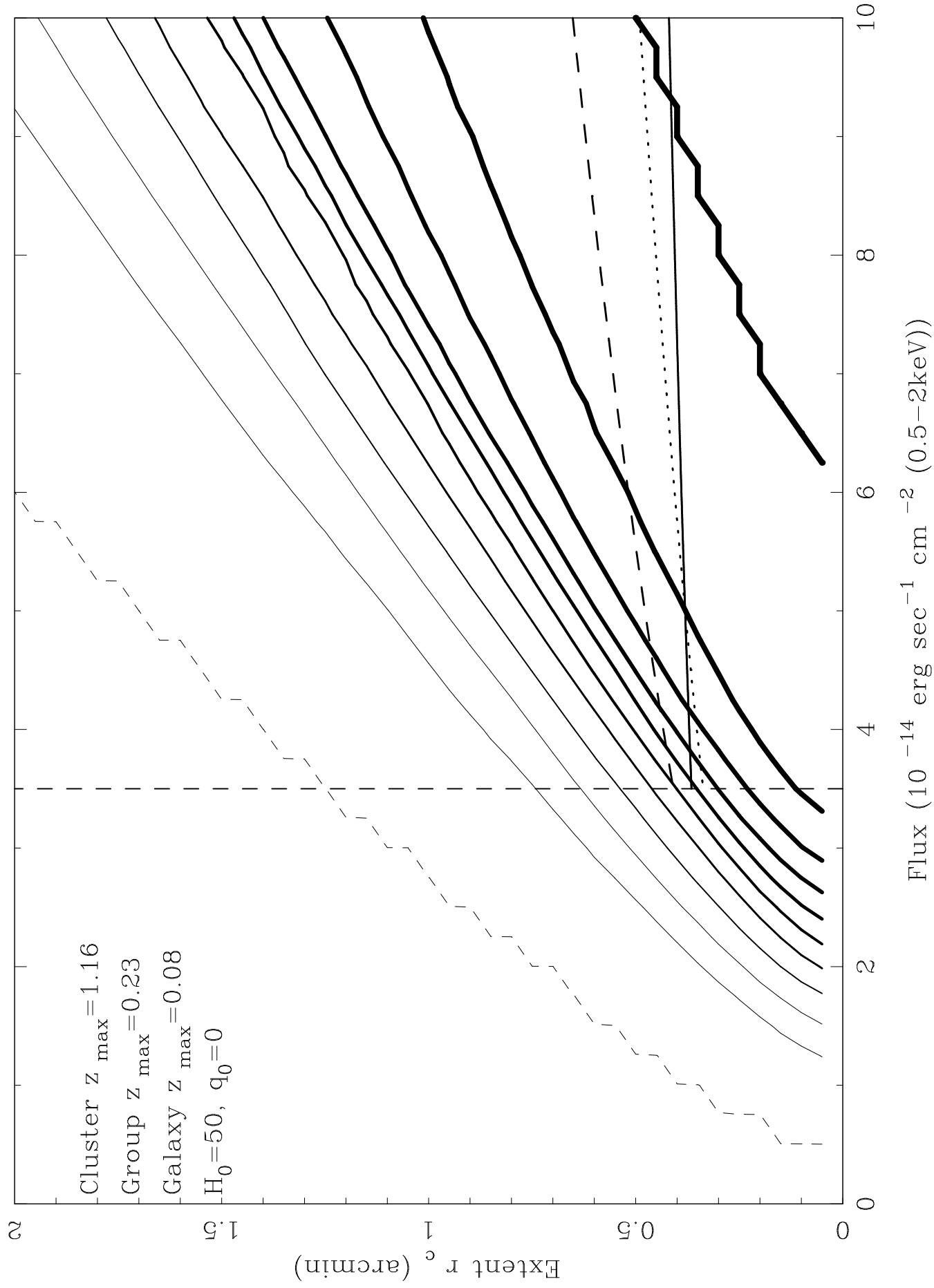
ra (pseudo)

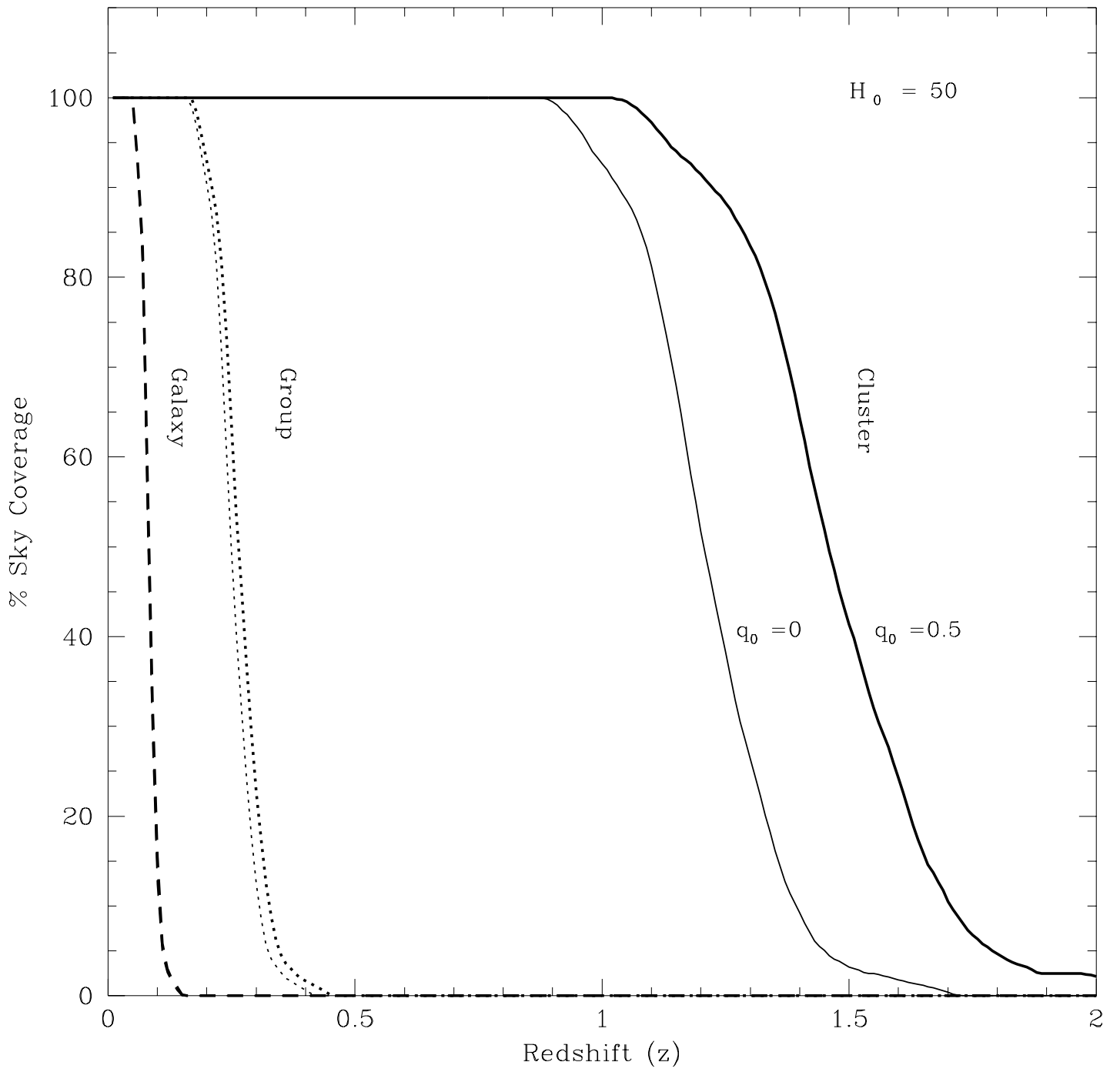




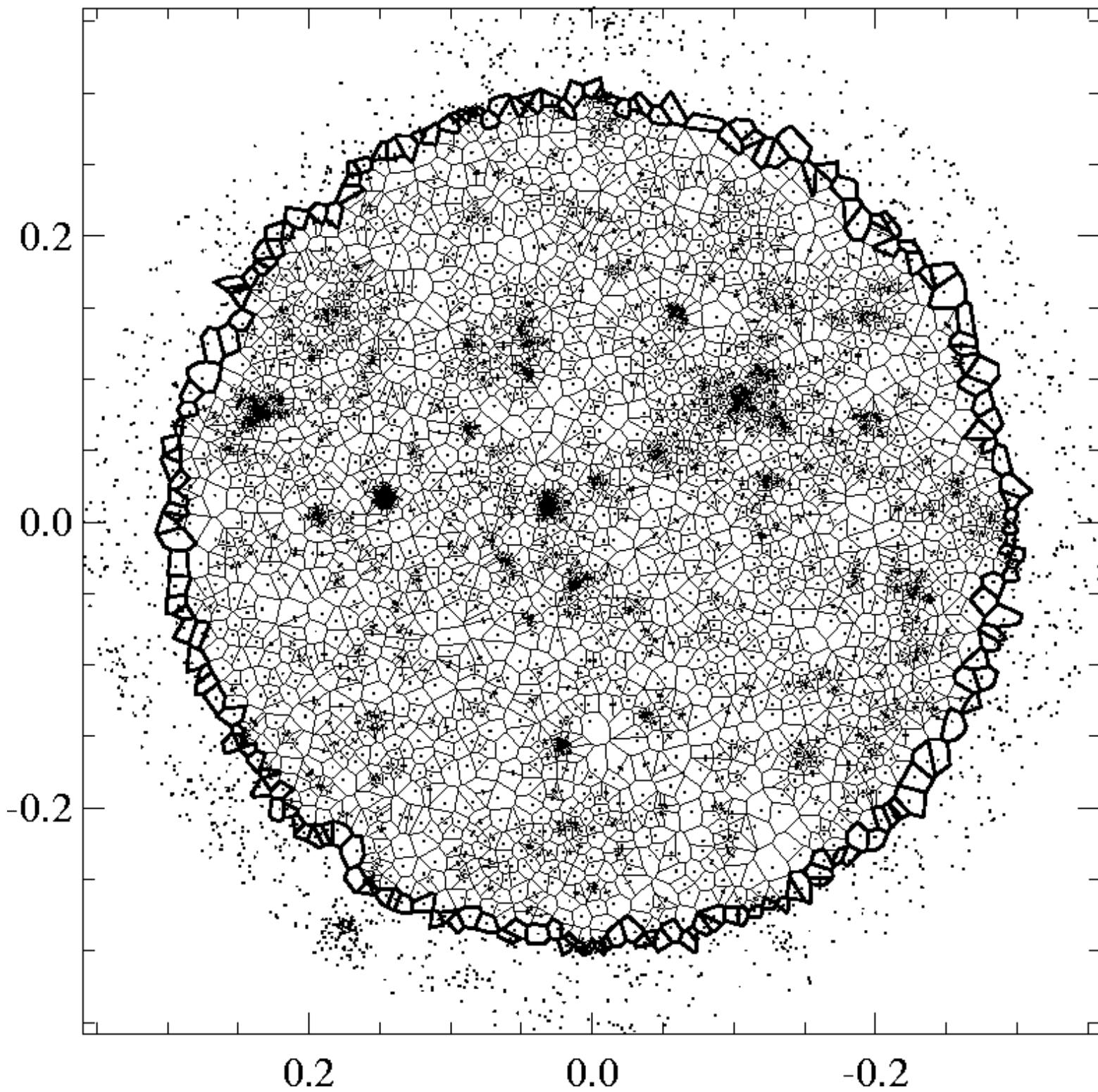


Sky coverage of WARPS

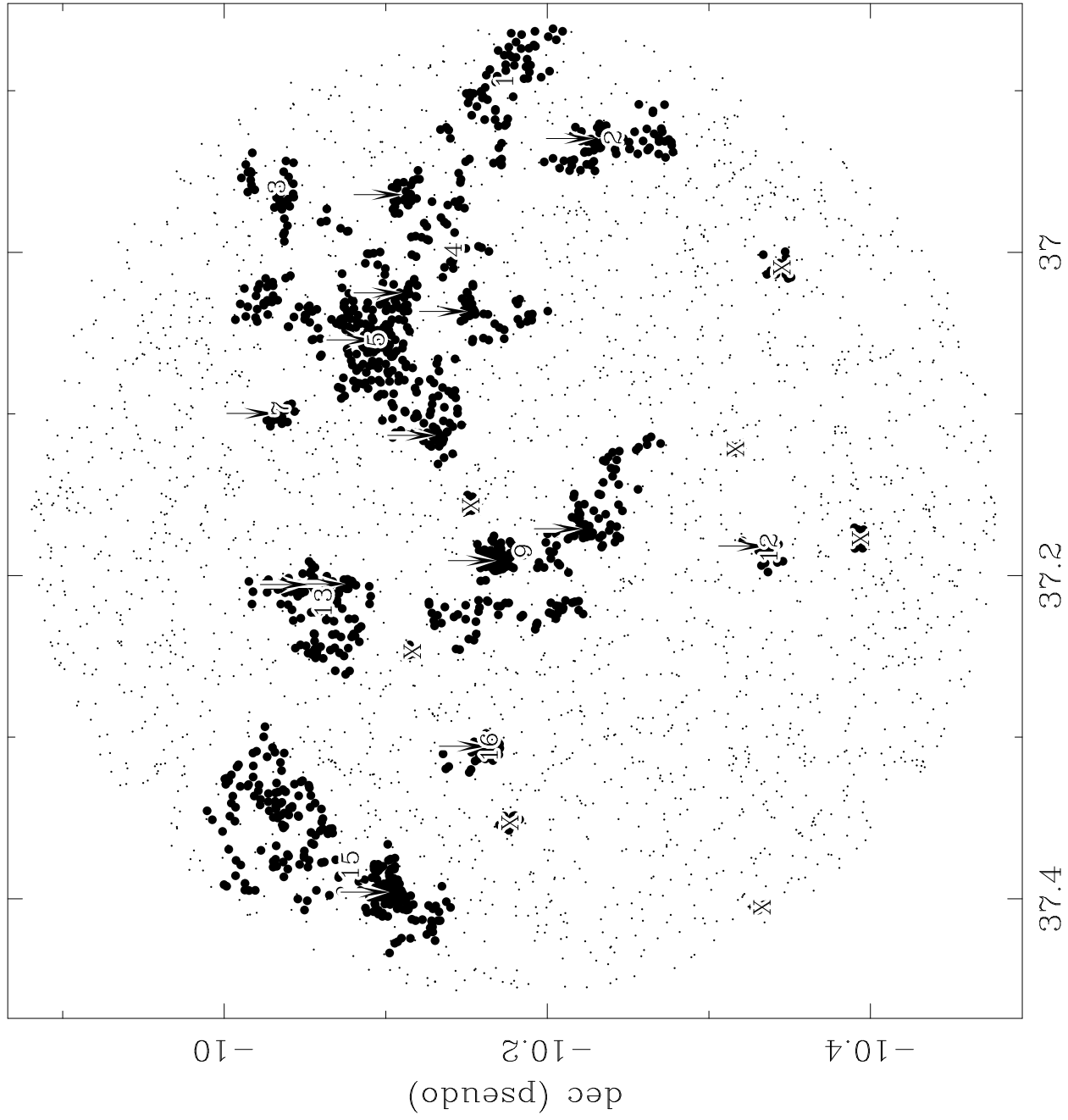




# US700114P.N1

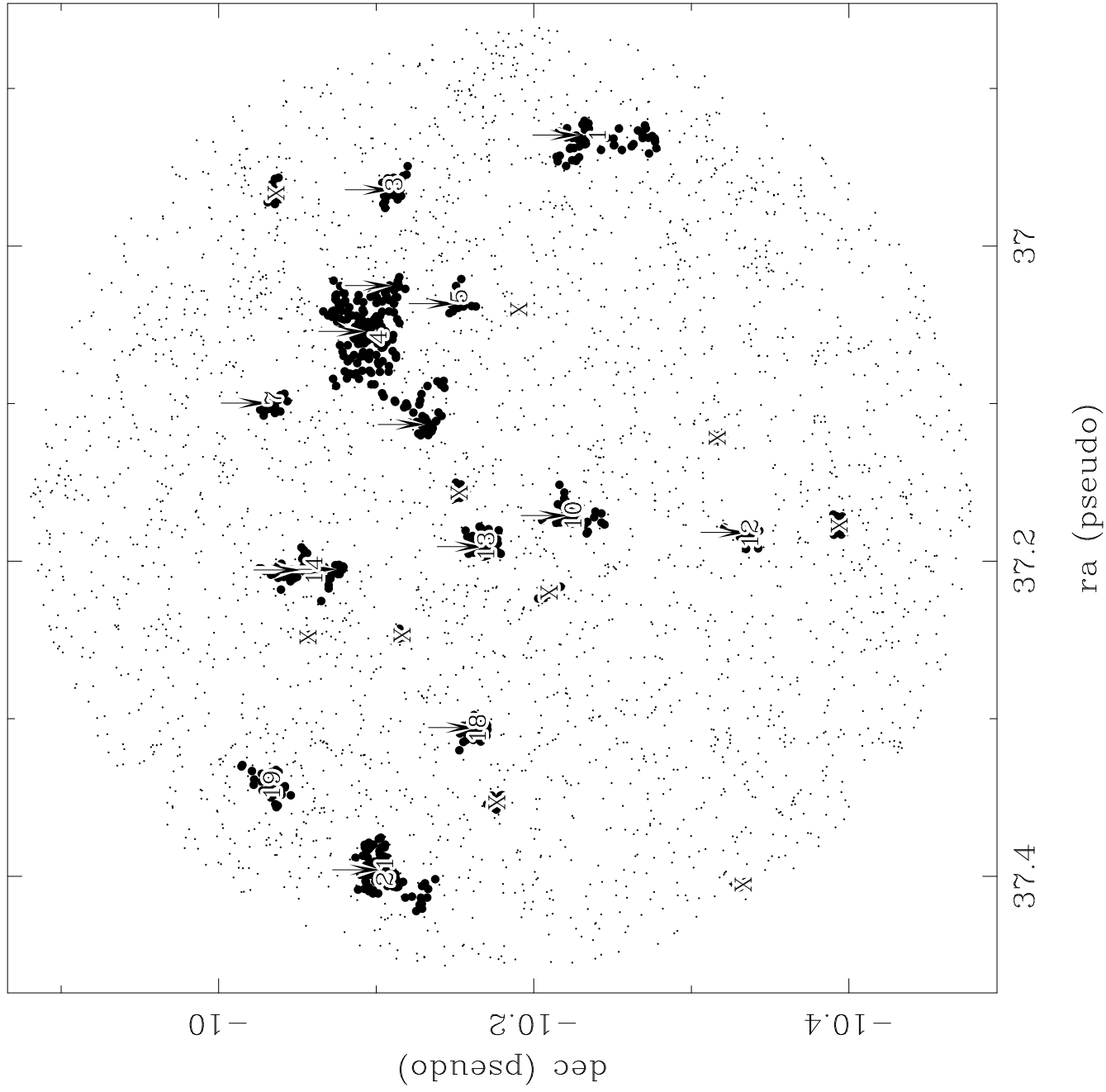


rp700114\_1.0

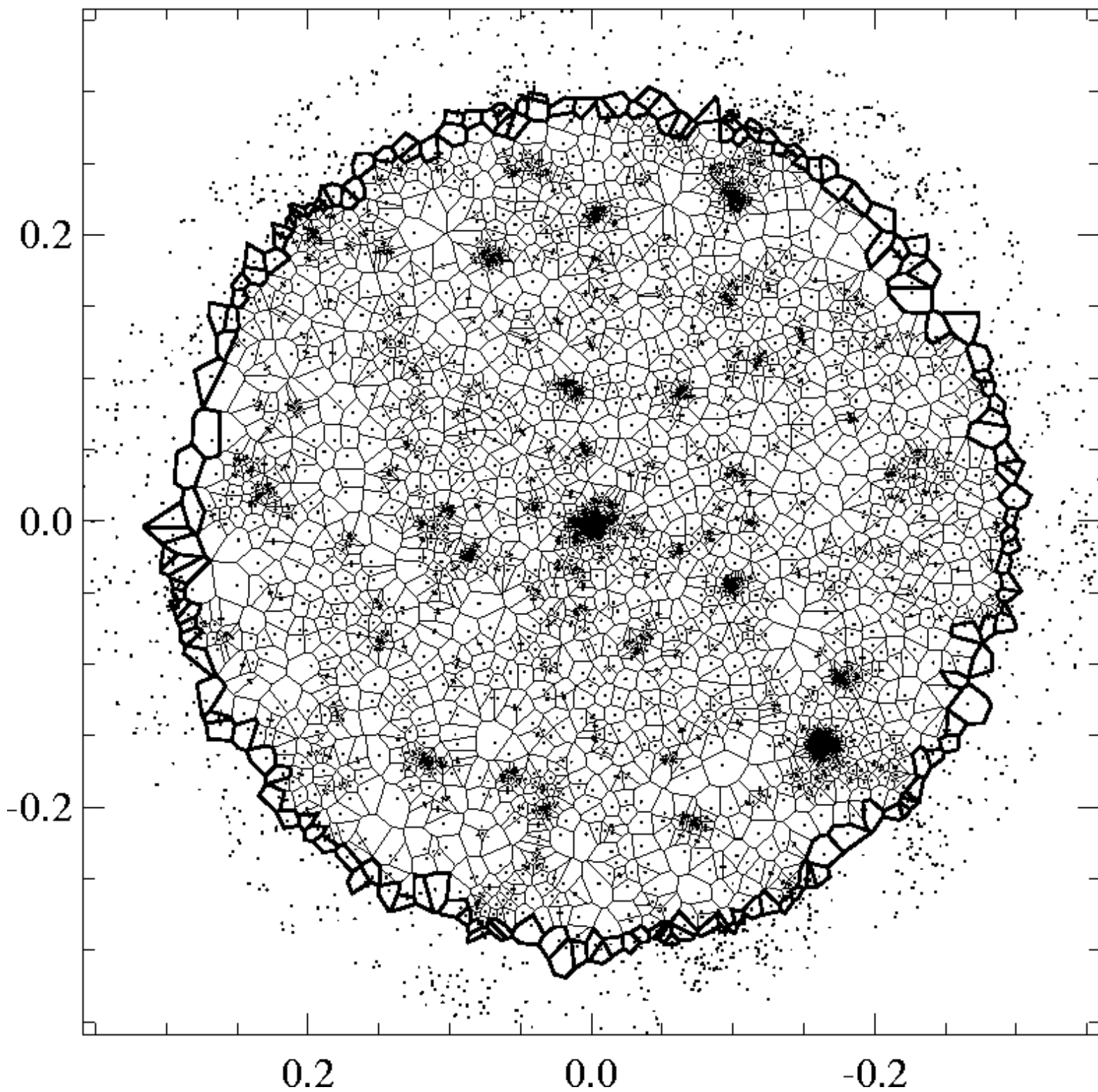


ra (pseudo)

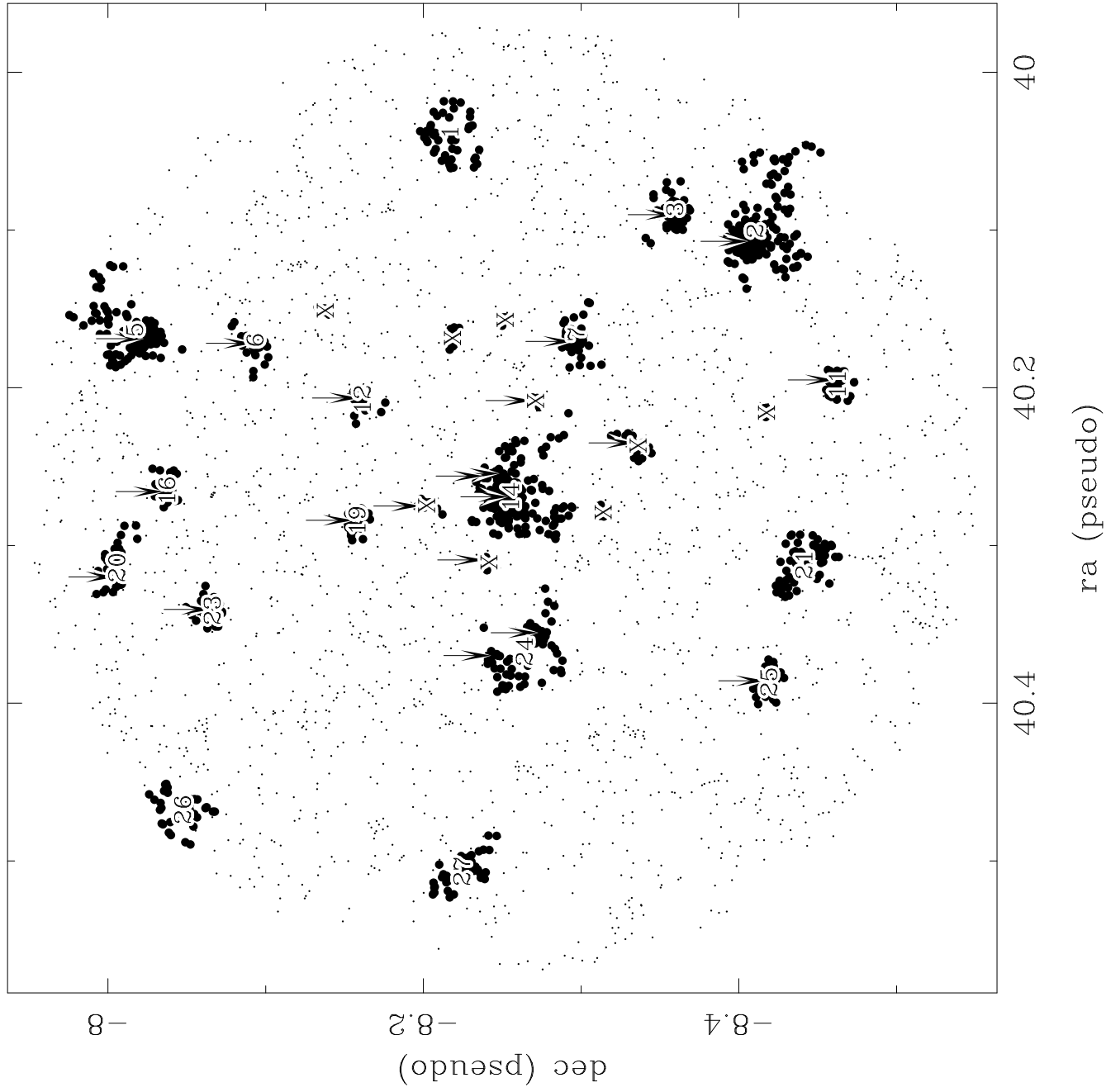
rp700114\_1.3



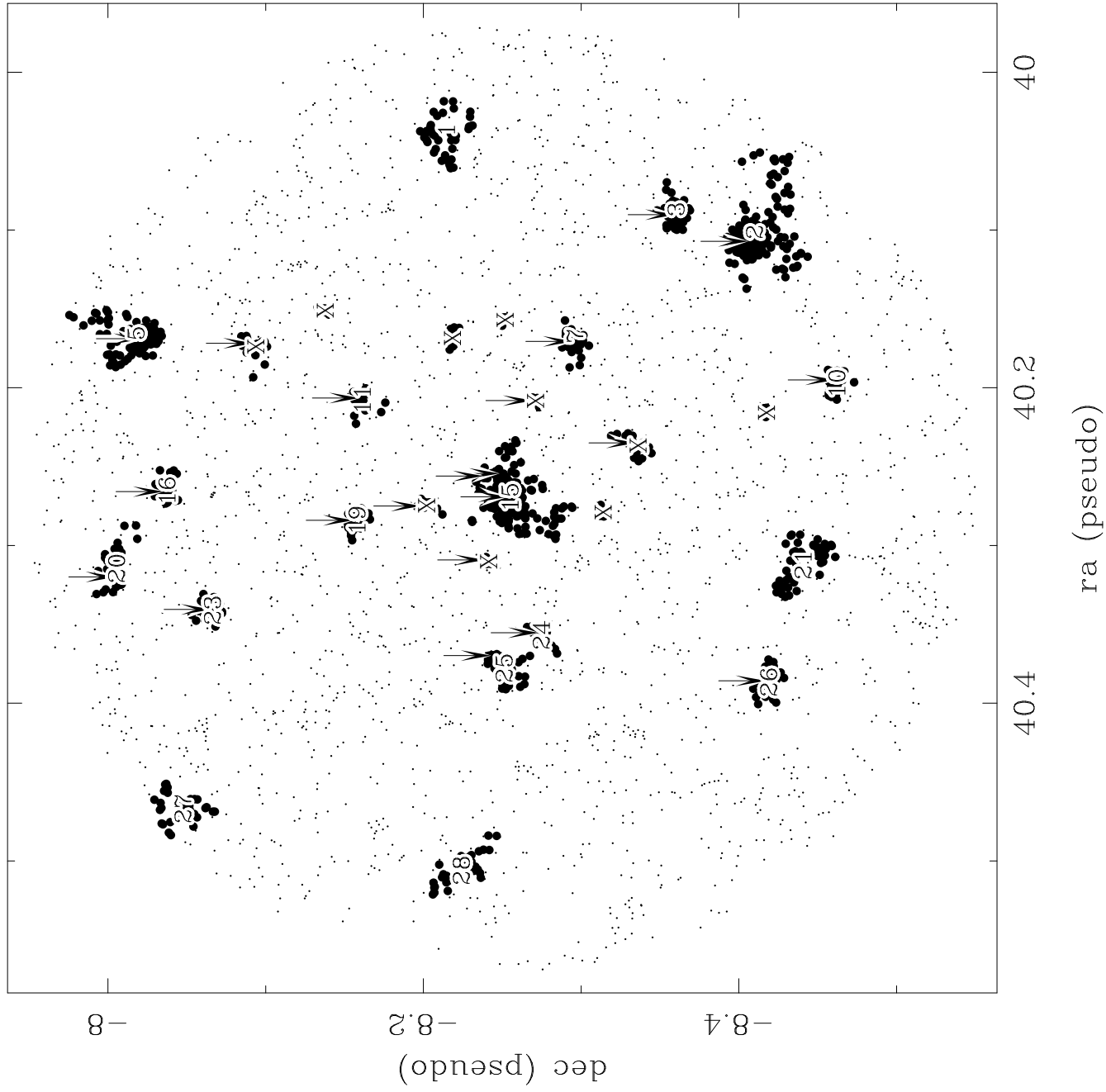
US600520P.N1



rp600520n00\_1.0



rp600520n00\_1.3



Distribution of WARPS surface brightness limits

